Prograde P-T Evolution of a Lawsonite Eclogite from the Monviso Meta-ophiolite (Western Alps): Dehydration and Redox Reactions during Subduction of Oceanic FeTi-oxide Gabbro

(Article begins on next page)

06 October 2024

UNIVERSITÀ DEGLI STUDI DI TORINO

Prograde *P–T* evolution of a lawsonite eclogite from the Monviso metaophiolite (Western Alps): dehydration and redox reactions during subduction of oceanic FeTi-oxide gabbro.

Chiara Groppo & Daniele Castelli

Dept. of Mineralogical and Petrological Sciences, University of Torino, via Valperga Caluso 35, I-10125, Torino, Italy.

Phone: +39 011 6705106
Fax: +39 011 6705128
Email: chiara.groppo@unito.it
          daniele.castelli@unito.it

Abstract
Lawsonite eclogites represent fossil records of processes occurring during subduction of cold and fast-subducting slabs, and provide the opportunity to investigate the thermal and metamorphic evolution of palaeosubduction zones. Occurrences of lawsonite eclogites are rare because lawsonite is often replaced during exhumation. We report here, for the first time, the occurrence of a lawsonite eclogite from the Monviso metaophiolite (Western Alps), representing the product of the Alpine metamorphism of a FeTi-oxide gabbro. The prograde metamorphic evolution of this lawsonite eclogite has been investigated using the petrologic approach of pseudosections. The reconstruction of its prograde *P–T* evolution allowed us to monitor changes in chemical and physical properties (mineral assemblages and compositions, density, H_2O content, oxygen fugacity) during subduction.

The pseudosection modelling suggests peak metamorphic conditions of $T \geq 550°C$, $P = 25\text{-}26$ kbar, and a decrease in the thermal gradient during subduction from about 9°C/km to less than 7°C/km, that may be interpreted as related to an increase in the subduction rate. During its prograde evolution, at a depth of about 65-70 km, the eclogite-facies metagabbro experienced a significant dehydration passing from the $Grt_1+Omp_1+Lws+Chl+Qtz+Rt$ assemblage (stage I) to the $Grt_2+Omp_2+Tlc+Qtz+Rt$ assemblage (stage II). The breakdown of lawsonite and chlorite caused the release of up to 3 wt% of H_2O and also of oxygen, as modelled by the redox-equilibrium $Lws+Qtz+Chl+Omp_1=Grt+Omp_2+H_2O+O_2$. This redox-equilibrium represents the boundary between an earlier, more-oxidized assemblage (stage I), stable at lower *T*, and a later, more-reduced assemblage (stage II), stable at higher *T*. These results have possible implications for the understanding of the complex interactions between crust and mantle in the subduction zones, especially in clarifying the processes locally involved in the oxidation of the mantle wedge overlying the subducting slab.

INTRODUCTION

Detailed petrological studies of prograde metamorphism in metaophiolites can provide important insights into the evolution of palaeosubduction zones, in terms of: (i) their thermal structures and evolution, and (ii) devolatilization reactions and metamorphic transformations occurring in the subducting slabs.

Several studies of heat flux and seismic activity carried out on present-day subduction zones (e.g. Royden & Husson, 2006; Schellart *et al.*, 2007) have shown that, in general, fast-subducting slabs are characterized by low thermal gradients, whereas slow-subducting slabs have higher thermal gradients (e.g. Peacock & Wang, 1999). Changes in the thermal structure of a subduction zone may result from changes in its subduction rate, in turn related to the complex interplay between density and geometry of the slab, and to the viscosity structure of the surrounding mantle (e.g. Royden & Husson, 2006). Variations in the subduction rates are widely reported from currently active subduction zones and may be also inferred for palaeosubduction environments on the basis of a careful reconstruction of the *P–T*–(t) evolution of metaophiolites (e.g. Groppo *et al.*, 2009a).

Devolatilization reactions, fluid-rock interactions and metamorphic transformations occurring in subducting slabs play a key role in revealing the complex physical-chemical transformations of crust and mantle at convergent margins. Fluids released from the variably hydrated subducting slab are, in fact, considered as the primary source of volatiles for arc magmatism and fluid-induced seismicity (e.g. Hawkesworth *et al.*, 1993; Parkinson & Arculus, 1999; Clift *et al.*, 2001; Kerrick & Connolly, 2001b; Peslier *et al.*, 2002; Forneris & Holloway, 2003; Hacker *et al.*, 2003; Spandler *et al.*, 2004). The dehydration history of the mafic portion of the subducting slab has been widely explored by high-pressure experiments since the last decades (e.g. Pawley & Holloway, 1993; Peacock, 1993; Yaxley & Green, 1994; Poli & Schmidt, 1995; Liu *et al.*, 1996; Schmidt & Poli, 1998; Molina & Poli, 2000; Forneris & Holloway, 2003; Dasgupta *et al.*, 2004; Dasgupta & Hirschmann, 2006; Poli *et al.*, 2009). Theoretical modelling of stable mineral assemblages at given *P–T* conditions has alternatively been used (e.g. Kerrick & Connolly, 1998, 2001a, b; Hacker *et al.*, 2003; Rüpke *et al.*, 2004). All these studies show that dehydration of the mafic portion of the subducting slab mainly occurs through continuous reactions that involve the breakdown of hydrated minerals at different depths. Although a significant fluid loss characterizes the shallowest portion of the subduction zone, variable amounts of H_2O are still retained in hydrous assemblages at higher depths (e.g. Poli & Schmidt, 1995; Kerrick & Connolly, 2001b; Hacker *et al.*, 2003; Poli *et al.*, 2009). Lawsonite is among the most important H_2O-reservoirs, being able to accommodate up to 11.5 wt% H_2O in its structure. Although lawsonite eclogites are predicted to be common at depths of 45-300 km in cold subduction zones (e.g. Poli & Schmidt, 1995; Kerrick & Connolly, 2001b; Hacker *et al.*, 2003), lawsonite seldom survives exhumation (e.g. Tsujimori *et al.*, 2006a; Ghent *et al.*, 2009) because its preservation requires that exhumation be accompanied by substantial cooling (e.g. Clarke *et al.*, 2006; Davis & Whitney, 2006, 2008). As a consequence, only about ten lawsonite-eclogite localities are currently known in Phanerozoic orogenic belts (see Tsujimori *et al.*, 2006b, for a review).

In the Western Alps, the Monviso metamorphic ophiolite represents one of the best preserved relics of the oceanic litosphere that formed during the opening of Mesozoic Western Alpine Tethys and underwent eclogite-facies metamorphism during the Alpine subduction. In spite of a number of papers devoted to the study of the magmatic protoliths and to the investigation of peak metamorphic conditions reached during Alpine subduction (Lombardo *et al.*, 1978; Philippot,

1988; Blake *et al.*, 1995; Messiga *et al.*, 1999; Schwartz *et al.*, 2000; Castelli *et al.*, 2002; Castelli & Lombardo, 2007), very few data are available so far on the prograde evolution of the Monviso metaophiolites.

In this paper, we have investigated the prograde metamorphic evolution of a very well preserved eclogitized FeTi-oxide gabbro from the Monviso metaophiolite, using the petrologic approach of isochemical *P–T* phase diagrams (or *P–T* pseudosections). The first peculiarity of this eclogite is the occurrence of lawsonite preserved in the prograde cores of both garnet and omphacite. These findings, reported here for the first time for the whole Monviso metaophiolite, represent an important contribution to the understanding of subduction and exhumation processes of metaophiolites from the Western Alps. The second peculiarity of the studied sample is its Fe-rich bulk composition, that allowed the development of Fe-rich garnet and omphacite, both characterized by a strong prograde chemical zonation, with iron in both the oxidation states. The petrological modelling of the studied sample, in the MnNCFMASHTO model system, allowed us:

(i)   to reconstruct the prograde evolution of the Basal Serpentinite Unit from the Monviso metaophiolite, not yet investigated so far. The obtained *P–T* trajectory, which lies inside the lawsonite eclogite-facies field, gives information about the thermal structure of the palaeosubduction zone, characterized by a decrease in the thermal gradient from 9 to 6-7°C/km.

(ii)   to monitor changes in chemical and physical properties (mineral assemblages, density, H_2O content) during subduction. We have investigated the main devolatilization reactions responsible for the dehydration of the metagabbro, and the consequences of dehydration process on the mineral assemblages and zoning.

(iii)   to obtain information about the redox reactions occurring in the metagabbro during subduction, with possible implication for the understanding of the complex interaction between crust and mantle in the subduction zones.

GEOLOGICAL SETTING

The Monviso metamorphic ophiolite is a composite body, structurally sandwiched between the underlying Dora-Maira Massif and the other, dominantly metasedimentary, units of the ocean-derived Piedmont Zone (Fig. 1a). It is one of the best preserved relics of the oceanic crust in the Western Alps that formed between ca. 170 and ca. 150 Ma (Rubatto & Hermann, 2003; Lombardo *et al.*, 2002) during opening of the Mesozoic Western Alpine Tethys and that underwent eclogite-facies metamorphism during the Eocenic Alpine subduction (45 ± 1 Ma – Rubatto & Hermann, 2003). It consists of two different types of units: (i) magma-rich units, in which a relatively thick basaltic layer caps gabbros and serpentinized peridotites (Vallanta, Forciolline, Viso Mozzo and Lago Superiore Units); (ii) magma-poor units in which serpentinized peridotites are directly covered by a thin sedimentary sequence (Passo Gallarino and Basal Serpentinite Units) (Fig. 1b, c) (Lombardo *et al.*, 1978; Lagabrielle & Lemoine, 1997; Castelli & Lombardo, 2007, with refs.).

Previous petrological works on the Monviso metaophiolite units were mainly dedicated to the estimate of peak *P–T* conditions experienced during subduction. *P–T* estimates were obtained for FeTi-oxide metagabbros, MgAl metagabbros, metabasalts and metaplagiogranites occurring at different structural positions, using different petrological approaches, i.e. conventional thermobarometry (Grt-Cpx and Grt-Phe thermometers, Jd-in-omphacite and Si-in-Phe barometers), *P–T* grids and average *P–T* methods of Thermocalc (Blake *et al.*, 1995; Messiga *et al.*, 1999; Schwartz *et al.*, 2000; Castelli *et al.*, 2002). Although all these studies concluded that peak

metamorphism occurred under very low thermal gradient (4-9°C/km), the estimated peak *P–T* conditions are not constant among the different units and range from a maximum of 620±50°C, 24±1 kbar (Messiga *et al.*, 1999 – Lago Superiore Unit) to a minimum of 450±50°C, 12±3 kbar (Schwartz *et al.*, 2000 – Viso Mozzo and Passo Gallarino Units). Blake *et al.* (1995) and Schwartz *et al.* (2000) documented a common exhumation history under blueschist-facies conditions for all the Monviso units. On the contrary, the prograde metamorphic evolution of the Monviso metaophiolite was never investigated and no lawsonite relics have been reported so far in any of the Monviso Units.

In the magma-poor, Basal Serpentinite Unit (BSU) of Varaita Valley, a primary plagiogranite - FeTi-oxide gabbro association is exposed (Fig. 1c), which testifies of an evolved tholeiite magma within ultramafic oceanic crust at late fractional crystallization stages (Castelli *et al.*, 2002; Castelli & Lombardo, 2007). Due to the Alpine tectono-metamorphic reworking, the plagiogranite was extensively recrystallized into fine-grained and massive, jadeite- + quartz ± phengite ± garnet ± ferroglaucophane rocks, locally cut by albite-quartz-bearing leucocratic layers that were interpreted as late-magmatic dikes. The FeTi-oxide gabbro, from which the studied sample was collected, was converted into omphacite + garnet + rutile ± glaucophane eclogite that forms a discontinuous envelope around the metaplagiogranite body or occurs as decimetre-thick folded boudins within the same metaplagiogranite. Preliminary *P–T* estimates (based on calculated phase compatibilities and phengite geobarometry) indicated $T > 575°C$ and $P > 19.5$ kbar for the peak Alpine assemblage in the metaplagiogranite body, in agreement with garnet-clinopyroxene geothermometry from the associated FeTi-oxide metagabbro samples which yielded $T = 545 ± 35°C$ at $P = 20$ kbar (Castelli *et al.*, 2002).

Mineral assemblages and bulk-rock compositions of the BSU metaplagiogranite - FeTi-oxide metagabbro association were given in Castelli & Lombardo (2007). The FeTi-oxide metagabbro samples (see inset in Fig. 1c for their location) are characterized by very similar microstructures (compare Fig. SM1, available as Supplementary Material), mineral assemblages and bulk-rock compositions (Castelli & Lombardo, 2007; see also Table 4). A detailed petrographic re-investigation of all the FeTi-oxide metagabbros (ten samples from the same area) allowed us to recognise, firstly in the Monviso metaophiolite, the occurrence of lawsonite relics in both garnet and omphacite cores of the OF2727 metagabbro sample.

PETROGRAPHY AND MINERAL CHEMISTRY

The FeTi-oxide metagabbro OF2727 is a fine-grained rock with an exceptionally preserved high-pressure assemblage. It consists of omphacite, garnet and rutile with minor blue amphibole and very minor lawsonite, talc and jadeite (Fig. 2: Figs. SM1 and SM2, available as Supplementary Material). Microstructural relics of the magmatic assemblage are represented by few millimetre-large clinopyroxene porphyroclasts, completely re-equilibrated as omphacite during the high-pressure metamorphic event, and by rutile aggregates grown at the expenses of interstitial magmatic ilmenite. Omphacite and rutile aggregates are slightly oriented to define a weak foliation. Representative analyses of garnet, clinopyroxene, amphibole, talc, lawsonite and chlorite are given in Tables 1-2; analytical methods are described in Appendix A. Mineral abbreviations are from Bucher & Frey (2002).

Both garnet and omphacite are strongly zoned (Figs. 2b-d, 3; Fig. SM3a-b available as Supplementary Material). Garnet occurs as small idioblasts (up to 0.5 mm in diameter) with reddish core (Grt_1) crowded of small inclusions of omphacite and minor lawsonite (Fig. 2e), glaucophane

and chlorite, and a pinkish rim (Grt_2) with minor, but larger, inclusions of omphacite and very minor talc. The textural zoning of garnet corresponds to a sharp chemical zoning. Mn shows a bell-shaped pattern typical of prograde zoning (X_{Mn} = 0.24→0.00 from core to rim), balanced by an increase in both X_{Mg} and X_{Fe} (X_{Mg} = 0.01→0.12, X_{Fe} = 0.56→0.82 from core to rim, respectively). Fe^{+3} shows the same bell-shaped trend as Mn, reaching the maximum values in the core ($Fe^{+3}/\Sigma Fe$ = 0.11) and progressively decreasing toward the rim ($Fe^{+3}/\Sigma Fe$ = 0.00). Ca zoning is more complex, slightly increasing from the inner core to the outer core and decreasing toward the rim (X_{Ca} = 0.21→0.27→0.11) (Fig. 3; Fig. SM4, available as Supplementary Material) [X_{Mn} = Mn/(Ca+Mg+Fe^{+2}+Mn); X_{Mg} = Mg/(Ca+Mg+Fe^{+2}+Mn); X_{Ca} = Ca/(Ca+Mg+Fe^{+2}+Mn); X_{Fe} = Fe^{+2}/(Ca+Mg+Fe^{+2}+Mn); $Fe^{+3}/\Sigma Fe$ = Fe^{+3}/(Fe^{+3}+Fe^{+2})]. The transition from the reddish core (Grt_1) to the pinkish rim (Grt_2) is marked by an abrupt decrease in X_{Ca} balanced by an increase in X_{Mg}. Locally, a slight increase in X_{Mn} suggests that partial resorption occurred at garnet rim (Fig. 3).

Four Na-clinopyroxene types, occurring in different microstructural sites, have been recognized. Omp_1 consists of scanty inclusions in the inner garnet core, with X_{Aeg} = 0.29–0.37, X_{Jd} = 0.22–0.26 and $X_{Mg}(Fe_{tot})$ = 0.36–0.44. A more jadeitic pyroxene (X_{Aeg} = 0.09–0.24; X_{Jd} = 0.58–0.69, in the following referred to as Jd_{ss}) occurs in the same microstructural position as Omp_1; although Jd_{ss} and Omp_1 rarely show equilibrium contacts (Fig. 2f), their occurrence in the inner garnet cores would suggest they were coexisting clinopyroxenes. Omp_2 occurs both in the deep green core of matrix nematoblasts (Fig. 2b) and as inclusions in garnet core (Grt_1) (Fig. 2e), whereas Omp_3 forms the light green rim of the matrix nematoblasts (Fig. 2b) and it is locally included in garnet rim (Grt_2) (Fig. 3). Omp_2 has higher X_{Aeg} and lower X_{Jd} and X_{Mg} [X_{Aeg} = 0.35→0.28; X_{Jd} = 0.25→0.35; $X_{Mg}(Fe_{tot})$ = 0.40–0.50; aegirine-augite according to the classification of Morimoto *et al.*, 1988] than Omp_3 [X_{Aeg} = 0.24→0.14; X_{Jd} = 0.35→0.45; $X_{Mg}(Fe_{tot})$ = 0.52–0.66] (Fig. 4 and Tables 1, 3) [X_{Aeg} = Fe^{+3}/(Fe^{+3}+Al^{VI}+Fe^{+2}+Mg); X_{Jd} = Al/(Fe^{+3}+Al^{VI}+Fe^{+2}+Mg); $X_{Mg}(Fe_{tot})$ = Mg/(Mg+Fe)]. The large clinopyroxene porphyroclasts, interpreted as microstructural relics of the magmatic assemblage, are patchly zoned omphacites, compositionally similar to either Omp_2 or Omp_3.

Blue amphibole (glaucophane according to the Na-amphibole classification of Leake *et al.*, 1997) is a minor phase occurring in two different microstructures: (i) rare prograde inclusions (Gln_1) occurring in the inner core of garnet, with $X_{Mg}(Fe_{tot})$ = 0.52–0.58, and (ii) a retrograde glaucophane occurring as small idioblasts (Gln_2) statically overgrowing the weakly oriented omphacite and rutile of the matrix (Fig. 2a) and showing the same composition of Gln_1.

Lawsonite is rare and mainly preserved as small inclusions in both garnet (Grt_1) and omphacite (Omp_2) cores (Figs. 2d-e). Larger lawsonite inclusions in garnet are generally replaced by fine-grained aggregates of epidote (Zo_{70-87}) and paragonite (Figs. 2e-g-h and 3). Lawsonite has not been observed in the matrix, either as preserved crystals or as its pseudomorphic replacements. Scanty talc (X_{Fe} = 0.15–0.19) is included both in the garnet rim (Grt_2) and in the omphacite porphyroclasts. Very rare chlorite flakes have been observed in the inner garnet core (Grt_1) (Fig. 3) and interpreted as preserved relics of a prograde assemblage. Finally, rare quartz has been observed as inclusions in both omphacite and garnet (Fig. 2b).

In spite of the relatively simple paragenesis, garnet and omphacite zoning together with the distribution of inclusions in garnet allow to define a prograde metamorphic evolution, which is summarized in Table 3. Two different pyroxenes (Jd_{ss} + Omp_1) were stable at relatively low-*T*, before and at the onset of garnet growth. Coexisting jadeitic pyroxene + omphacite pairs in natural

assemblages are rare (e.g. Matsumoto & Hirajima, 2005; Tsujimori $et\ al.$, 2005, 2006a, b; Miyazoe $et\ al.$, 2009) and often due to the presence of a T- dependent miscibility gap approximately located at Jd_{60}–Jd_{85}, (e.g. Green $et\ al.$, 2007). Compositions of Omp_1 (Jd_{22-26}) and Jd_{ss} (Jd_{58-69}) in sample OF2727 lie outside this generally accepted miscibility gap. These compositions could be alternatively due to "mosaic equilibrium" phenomena (i.e. Jd-rich and Jd-poor clinopyroxenes grew in the former plagioclase- and pyroxene- microdomains, respectively) (e.g. Korzhinskii, 1959). Garnet core (Grt_1) then grew in equilibrium with a single omphacitic clinopyroxene (Omp_2), lawsonite and rutile, whereas the growth of garnet rim (Grt_2) coincides with: (i) a change in the omphacite composition (Omp_3), (ii) the disappearance of lawsonite and (iii) the development of talc. Na-amphibole (Gln_2) is a later phase, statically overgrowing the prograde- and peak-parageneses.

PSEUDOSECTION MODELLING

Pseudosection modelling is currently recognized as one of the most powerful method to gain thermobarometric information on rocks, because it provides a framework to interpret both textural information and mineral compositions in terms of P–T evolution (e.g. Powell & Holland, 2008). The mafic system has been widely investigated in the last decades (e.g. Clarke $et\ al.$, 1997, 2006; Will $et\ al.$, 1998; Carson $et\ al.$, 1999; Štípská & Powell, 2005; Davis & Whitney, 2006, 2008; Groppo $et\ al.$, 2007, 2009a) but until few years ago modelling of Fe^{+3}-bearing systems was hampered by the lack of solid-solution models for Fe^{+3}-bearing mineral end-members (Will $et\ al.$, 1998; Wei $et\ al.$, 2003). Following the pioneering work of Warren & Waters (2006) on Fe^{+3}-bearing eclogites and blueschists from Oman, and thanks to recent improvements in the solution models of omphacite (Green $et\ al.$, 2007) and amphibole (Diener $et\ al.$ 2007), oxidized systems begin to be successfully investigated (e.g. Groppo $et\ al.$, 2009b; Wei $et\ al.$, 2009). We have therefore used this approach and details on the pseudosection calculations are given in Appendix B.

Bulk-rock composition

Bulk-rock composition of sample OF2727 has been estimated by two different methods: (i) average of 15 SEM-EDS analyses of 4.70×3.20 mm selected areas within a polished thin section, and (ii) combining mineral modes and compositions (see Appendix A, Table SM1 and Fig. SM2 for details). These compositions have been compared with the ICP-MS analysis of the same sample (Castelli & Lombardo 2007, their Table 2). Bulk compositions obtained with methods (i) and (ii) are very similar and both slightly differ from the ICP-MS analysis for their lower CaO and Al_2O_3 contents (Table 4, Fig. SM4 available as Supplementray Material). These little differences may account for the presence of scanty epidote-bearing domains in the hand specimen crushed for ICP-MS analysis, in analogy with those observed in other samples collected from the same area. We have therefore used the bulk composition after method (i) because of its statistical significance and the better microstructural control. Bulk compositions of other FeTi-oxide metagabbros from the Western Alps (Monviso metaophiolites: Castelli & Lombardo, 2007; Lanzo and Rocciavrè massifs: Pognante $et\ al$., 1982, Pognante & Toscani, 1985; Aosta Valley: Bocchio $et\ al.$, 2000) are reported for a comparison in Table 4 and Fig. SM4.

Fractionation effects on the bulk-rock compositions

The occurrence of strongly zoned garnet porphyroblasts likely caused chemical fractionation of the bulk-rock composition, due to the preferential sequestration of some elements in the garnet cores. In

this case a single pseudosection, calculated on the base of the bulk-rock composition, is inadequate to model the entire evolution of the rock: modelling separate pseudosections using the effective composition representative of each equilibration volume will result in a much more accurate reconstruction of the P–T path. Several methods have been proposed to calculate the effective bulk composition modified because of elemental partitioning related to garnet growth (Stüwe, 1997; Marmo *et al.*, 2002; Evans, 2004; Zuluaga *et al.*, 2005; Gaidies *et al.*, 2006; Groppo & Rolfo, 2008; Groppo *et al.*, 2009a). For the studied sample, bulk compositions effectively reacting during each stages of garnet growth have been calculated following the method described by Evans (2004) and Gaidies *et al.* (2006). This method applies a Rayleigh fractionation model based on measured Mn content of garnet and requires that a strong correlation between the concentration of Mn vs. Fe, Mg and Ca in garnet exists. In order to model the bulk-composition fractionation as a continuous process, several growth increments should be considered for garnet (in other words, the more the growth increments used, the more detailed will be the modelling of fractionation effects). For this reason, garnet zoning has been divided in eight growth shells, on the basis of the Mn content and the core vs. rim size (Fig. SM5a, available as Supplementary Material). Garnets with the highest and similar MnO contents have been selected as representative of garnet crystals sectioned through the actual core. Garnet core has been divided in five shells ($Grt_{1a \to e}$), while garnet rim has been divided in three shells ($Grt_{2a \to c}$). The studied sample shows significant fractionations effects (Fig. SM5, available as Supplementary Material) and eight different bulk compositions have been then considered (Table 4), representative of equilibrium compositions during the growth of $Grt_{1a} \to Grt_{2c}$.

Although omphacite is also zoned, bulk-composition fractionation due to its growth has not been considered, mainly because the compositional differences between Omp_2 and Omp_3 are much less pronounced with respect to those between Grt_1 and Grt_2.

Estimation of Fe_2O_3 in the modelled bulk compositions

The bulk $Fe_2O_3/(FeO+Fe_2O_3)$ ratio [in the following referred to as $X(Fe_2O_3) = Fe_2O_3/(FeO+Fe_2O_3)$ mol%] appears to change during the rock metamorphic evolution as testified by the different Fe^{+3} content in the omphacite and garnet cores (Omp_2, Grt_1) and rims (Omp_3, Grt_2), respectively. Omphacite and garnet zoning suggests that the $X(Fe_2O_3)$ decreased during the rock evolution; moreover, the abrupt transition from Grt_1 to Grt_2 and from Omp_2 (included in Grt_1) to Omp_3 (included in Grt_2) suggests that the decrease in $X(Fe_2O_3)$ occurred rapidly and discontinuously and coincides with the transition from garnet core to garnet rim (i.e. stages I→II of Table 3). As a consequence, the $X(Fe_2O_3)$ ratio in the bulk-rock composition cannot be directly measured from the sample, because $X(Fe_2O_3)$ values obtained by conventional bulk-methods (e.g. wet chemical determination) or by combining mineral modes and compositions are not representative of equilibrium composition at each modelled stage of the metagabbro evolution.

The $X(Fe_2O_3)$ during stages I and II was therefore estimated using a "best-fit" criterion between modelled isopleths and measured compositions of garnet and omphacite. More in detail, several P–T pseudosections have been calculated using different $X(Fe_2O_3)$ values, ranging from $X(Fe_2O_3) = 0.10$ to $X(Fe_2O_3) = 0.25$ mol%. For each stage, the $X(Fe_2O_3)$ ratio has been considered correct when the modelled compositional isopleths of both garnet and omphacite intersect each others, fitting the measured mineral compositions. Conversely, if the observed mineral assemblages and compositions are not matched by a field in the pseudosection, this indicates that the composition of the equilibration volume has been incorrectly assigned (Powell & Holland, 2008).

Fig. SM6a, b (available as Supplementary Material) show that for $X(Fe_2O_3) \leq 0.15$ and $X(Fe_2O_3) \geq 0.25$ mol%, Grt_1 and Omp_2 compositional isopleths do not show any intersection, whereas for $X(Fe_2O_3) = 0.20$ mol%, the modelled Grt_1 and Omp_2 compositional isopleths intersect themselves in the omphacite + chlorite + garnet + lawsonite + quartz + rutile field, which is consistent with the inferred prograde assemblage (cf. Table 3). Therefore, in order to model the stage I P–T conditions, corresponding to the growth of garnet and omphacite cores (Grt_1 and Omp_2) a $X(Fe_2O_3) = 0.20$ mol% has been used. The stage II P–T conditions, corresponding to the growth of garnet and omphacite rims (Grt_2 and Omp_3), has been modelled using a lower $X(Fe_2O_3) = 0.15$ mol%, for which the modelled Grt_2 and Omp_3 isopleths intersect themselves (Fig. SM6a).

For comparison, the $X(Fe_2O_3)$ values measured on the whole sample using two different techniques – wet chemistry and mineral modes and compositions (see Appendix A for further details) – are reported in Table 4. The wet chemistry method (data from Castelli & Lombardo, 2007) gives a $X(Fe_2O_3)$ slightly higher (0.25 mol%) than those estimated using the "best-fit" criterion (0.20 and 0.15 mol% for stages I and II, respectively), and this is consistent with the presence of scanty epidote-bearing domains in the sample crushed for wet chemistry analysis, as previously suggested. Similar $X(Fe_2O_3)$ values, in the range of 0.12–0.26 mol% are also reported for other Fe-Ti oxide metagabbros from the Monviso metaophiolites (Castelli & Lombardo, 2007 and Table 4) and from the Aosta Valley in the Western Alps (Bocchio *et al.*, 2000). Conversely, the $X(Fe_2O_3)$ value measured by combining mineral modes and compositions (0.17 mol%, Table 4) is intermediate between those estimated for stage I and stage II, thus confirming the reliability of the two values here adopted by using the "best-fit" criterion.

RESULTS
The prograde *P*–*T* path
Eight different pseudosections (1a-1e and 2a-2c for stages I and II, respectively) have been modelled for the studied sample, based on different bulk compositions representing equilibrium compositions during the growth of $Grt_{1a} \rightarrow Grt_{2c}$ (cf. Table 4) and, as explained above, at $X(Fe_2O_3) = 0.20$ and $X(Fe_2O_3) = 0.15$, respectively. Modelled compositional isopleths of garnet (X_{Ca} and X_{Mg}) and omphacite (X_{Aeg}) have been used to constrain P–T conditions of garnet growth, from stage I (Grt_{1a-e} and Omp_2) to stage II (Grt_{2a-c} and Omp_3). Results are given in Figs. 5, SM7a-d (available as Supplementary Material) and summarized in Fig. 6. The estimated modal amounts of each phases and the H_2O wt% are also reported in Table 5. Garnet compositions provide good constraints on temperatures, whereas pressures are better constrained for stage I (Grt_{1a-e}) with respect to stage II (Grt_{2a-c}) (Fig. 5, 6 and Table 5), for which X_{Ca} and X_{Mg} isopleths of garnet cut at smaller angles.

Pseudosection modelling shows that the studied eclogite well preserves the metamorphic assemblages that developed along a segment of its subduction path from about 420°C, 16 kbar to 550°C, 25–26 kbar (Fig. 6). The modelled peak temperature must be considered as a minimum, because garnet is partially resorbed at its rim (Fig. 3) and the highest X_{Mg} values may have been possibly resetted during (the albeit scanty) retrogression. As a consequence of this P–T trajectory, the eclogite-facies metagabbro passed from the hydrated Grt+Omp+Lws+Chl+Qtz+Rt assemblage (stage I) to the nearly anhydrous Grt+Omp+Tlc+Qtz+Rt assemblage (stage II). More in detail, the transition from stage I to stage II (i.e. from Grt_{1e} to Grt_{2a}) corresponds to an abrupt decrease of the modelled water content in the system ($H_2O = 3.5 \rightarrow 1.7$ wt%, see Table 5 and Fig. 7a), marked by

the complete destabilization of lawsonite and chlorite that also accounts for an abrupt increase in density (Table 5, Fig. 7b).

Our pseudosections in the given $P–T$ range do not model two microstructural observations: (i) the coexistence of Omp_1 and Jd_{ss} in the inner garnet core (Grt_{1a-b}), interpreted as earlier than garnet growth, and (ii) the stability of Gln_1 in the same metamorphic stage. However, additional $P–T$ pseudosection modelling at lower pressure and temperature shows that two clinopyroxenes and glaucophane are stable at $P < 14$ kbar and $T < 300°C$, suggesting that Omp_1, Jd_{ss} and Gln_1 are relics of a prograde assemblage that developed during an earlier stage of subduction.

The studied sample provides little information on its retrograde evolution. Glaucophane in the matrix (Gln_2), which has been interpreted as an early retrograde phase on the basis of microstructural evidence, is predicted to be stable at T slightly higher than the modelled peak conditions (Am in Fig. 5c) and the Gln-in curve has a positive slope. Considering that the modelled peak temperature must be considered as a minimum, the growth of glaucophane appears to be compatible with the very early stages of retrogression at $P < 23$ kbar and $T < 560°C$. Finally, most of the coarse-grained lawsonite included in garnet has been replaced by epidote + paragonite aggregates (Fig. 2e-g-h). The presence of paragonite in the breakdown assemblage of lawsonite suggests that the reaction is not isochemical. Lü *et al.* (2009) suggested that the required Na could derive from the jadeite component of the frequent omphacite inclusions in garnet, according to the reaction: Lws + Jd = Czo + Pg + Qtz + H_2O. There is no evidence of such reaction in the OF2727 sample, however it is worth noting that epidote + paragonite aggregates replaced the coarser-grained lawsonite inclusions, which were most likely polymineralic, whereas the finer-grained monomineralic inclusions are still preserved.

The dehydration reactions

The modelled H_2O amounts at each stage are summarized in Table 5 and Fig. 7a. These data show that the dehydration of the system mainly occurred at the transition between stage I and stage II (Fig. 7a), i.e. at the highest T-side of the quini-variant Lws+Qtz+Chl+Omp+Grt+Rt field (Fig. 5b, composition 1e), where the H_2O content decreases from about 3.5 wt% to less than 1.7 wt% (Table 5 and Fig. 7a). The devolatilization reactions responsible for this significant dehydration have been calculated for composition 1e in the simplified system NCFMASTHO at $460<T<500°C$, $20<P<22$ kbar (i.e. the $P–T$ conditions estimated for the growth of Grt_{1e}). More details on the calculations of dehydration and redox reactions are given in Appendix C.

Due to the approximation by discrete steps of the continuous compositional variation of the phases involved (garnet, omphacite and chlorite), the dehydration reactions appear as pseudo-univariant equilibrium curves (Connolly & Kerrick, 1987). Two types of pseudo-univariant equilibria occur in the Lws+Qtz+Chl+Omp+Grt+Rt field (Fig. 8):

(A) Lws + Qtz + Omp_1 + Chl = Omp_2 + Grt + H_2O;

(B) Lws + Qtz + Chl_1 + Omp_1 = Chl_2 + Omp_2 + Grt + H_2O.
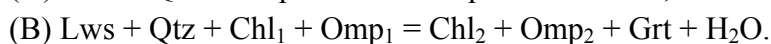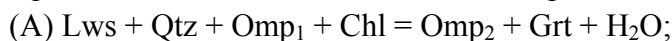
Type (A) equilibria are responsible for the breakdown of both lawsonite and chlorite, whereas type (B) equilibria involve the breakdown of lawsonite and a chemical re-equilibration of both omphacite and chlorite. In both equilibria types garnet only occurs as a product, and quartz (present in very low amount) is completely consumed. The H_2O content of the system rapidly decreases from > 3.5 wt% to < 1.4 wt% (Fig. 8). For both equilibria types (A) and (B), the breakdown of lawsonite and chlorite is associated to the growth of garnet and to a significant chemical re-equilibration of omphacite. Compositions of both reactant and product phases vary across the

Lws+Qtz+Chl+Omp+Grt+Rt field: at increasing temperature, Chl_2 is Mg-richer than Chl_1 and, in agreement with the measured compositions, Omp_2 is enriched in the diopsidic component and depleted in the aegirine component with respect to Omp_1, whereas garnet is progressively enriched in the pyrope component (Fig. 8). Intersections between type (A) and (B) pseudo-univariant curves are pseudo-invariant points that mark a change in composition of chlorite and omphacite along type (A) and (B) equilibria, respectively.

Redox reactions during subduction

In order to evaluate the redox reactions occurring during the dehydration of the system, an isobaric T-log$f(O_2)$ projection has been calculated at P = 21 kbar (i.e. at pressure averaging the growth of Grt_{1e}) in the simplified system NCFMASTHO (Fig. 9) (see Appendix C for further details).

Because P has been fixed, the pseudo-univariant dehydration equilibria (A1-A9, B1-B4) of Fig. 8 correspond to pseudo-invariant points in Fig. 9, and they univocally define the log$f(O_2)$ of the assemblage at given P and T. Changing pressure has a very little influence on the position of pseudo-invariant points [±0.1 log$f(O_2)$ units for ΔP = ±1 kbar]. Fig. 9 shows that the log$f(O_2)$ of the system progressively increases [log$f(O_2)$=-22.8→-20.9] with increasing temperatures from stage I to stage II (i.e. the observed $Grt_{1\to2}$ and $Omp_{2\to3}$ transition).

The pseudo-invariant points (A1-A9, B1-B4) in the T-log$f(O_2)$ projection of Fig. 9 are connected by pseudo-univariant equilibria ($r1$-$r12$) that define the more general equilibrium: $Lws+Qtz+Chl_{ss}+Omp1_{ss}= Grt_{ss}+Omp2_{ss}+H_2O+O_2$. The broken shape of this equilibrium is due to the approximation of the continuous variation in the solid-solution compositions by discrete steps (pseudocompounds). Equilibria $r1$-$r12$ correspond to devolatilization reactions that produce H_2O and O_2 up-temperatures, and divide the T-log$f(O_2)$ space in two fields: on the more oxidized side of the diagram the $Lws+Qtz+Omp_1+Chl_1$ assemblage is stable, whereas on the more reduced side is stable the $Grt+Omp_2+H_2O+O_2$ assemblage. Moving along this equilibrium from 460°C to 500°C, chlorite, omphacite and garnet progressively change their compositions. Crossing the $Lws+Qtz+Chl_{ss}+Omp1_{ss}= Grt_{ss}+Omp2_{ss}+H_2O+O_2$ equilibrium towards higher-T, H_2O and O_2 are released. Particularly: (i) for one mole of lawsonite + chlorite consumed up-T, about 2.0-2.7 moles of H_2O are released on average, and (ii) for one mole of omphacite ($Omp2_{ss}$) produced up-T, about one mole of oxygen is released on average (Fig. 9). As a consequence, the resulting assemblage ($Grt_{ss}+Omp2_{ss}$) at T = 500°C is less hydrated and less oxidized than the initial one ($Lws+Qtz+Chl_{ss}+Omp1_{ss}$) at T = 460°C, accounting for the sharp compositional variation in both omphacite and garnet from stage I to stage II. This means that the $Lws+Qtz+Chl_{ss}+Omp1_{ss}= Grt_{ss}+Omp2_{ss}+H_2O+O_2$ equilibrium represents the boundary between a more oxidized assemblage (at lower T) and a more reduced assemblage (at higher T).

Reliability of the results

The approach used to infer the P–T–fO_2 conditions attained during the subduction of the Monviso FeTi-oxide metagabbro deserves some words of caution about the following points:

(i) Although we have demonstrated that a small amount of ferric iron occurs in garnet, the "well-constrained" Fe^{+3}-free solution model of Holland & Powell (1998) has been preferred for pseudosection calculations with respect to the Fe^{+3}-bearing model of White *et al.* (2007). This latter model, in fact, has been developed in the pelitic NCKFMASHTO system and the authors themselves warn that the introduction of the end-member thermodynamics and *a–x* relationships for

spessartine will likely give unreliable or erroneous results if used in conjunction with their model. As garnet cores in the studied sample are considerably richer in Mn than in Fe^{+3}, we have preferred to neglect the influence of Fe^{+3} for the stabilization of garnet. This choice mainly affects the *P–T* conditions estimated for the Grt_1 growing stages, which contain the maximum Fe^{+3} contents (especially Grt_{1a-c}, for which $Fe^{+3}/\Sigma Fe>0.05$), and probably results in some underestimation of the *P–T* conditions (about 1 kbar and 10°C, respectively) inferred for the growth of garnet core.

(ii) The $Fe^{+3}/\Sigma Fe$ ratio in omphacite has not been directly measured but only calculated by stoichiometry from EMP analyses. Previous studies (e.g. Sobolev *et al.*, 1999; Schmid *et al.*, 2003; Proyer *et al.*, 2004) have demonstrated that in many cases there is no direct correlation between EMP-calculated values and values measured using other techniques such as Mössbauer or micro-XANES spectroscopies. This could obviously affect the validity of our results, which are also based on the best fit between modelled and calculated omphacite compositions. In omphacite, the precision in determination of SiO_2 and Na_2O largely controls the $Fe^{+3}/\Sigma Fe$ values based on stoichiometry (e.g. Sobolev *et al.*, 1999). Omphacite crystals in the studied sample have been analysed using both WDS and EDS techniques, with different analytical conditions and calibration standards: the X_{Aeg} and X_{Jd} ratios calculated by stoichiometry from the two set of analyses are comparable (WDS - Omp_2: X_{Jd} = 0.24–0.34, X_{Aeg} = 0.30–0.35; Omp_3: X_{Jd} = 0.36–0.38, X_{Aeg} = 0.17–0.18; EDS - Omp_2: X_{Jd} = 0.28–0.32, X_{Aeg} = 0.31–0.33; Omp_3: X_{Jd} = 0.38–0.39, X_{Aeg} = 0.18–0.19). In addition, special care has been used in determining the Na content using the WDS technique, by decreasing the acquisition time to avoid Na loss. We are therefore confident that the calculated $Fe^{+3}/\Sigma Fe$ ratios are reliable approximation of the actual redox state of omphacite.

(iii) Pseudosetion modelling suggests that chlorite was stable during the prograde evolution. As is the case for other phyllosilicates, the substitution of Al^{+3} for Fe^{+3} may also occur in chlorite and the presence of Fe^{+3} will affect the activity of chlorite end-members. However, it has been neglected in the modelling due to the lack of thermodynamic data for the Fe^{+3}-chlorite end-member. Vidal *et al.* (2006) demonstrated that there is a strong correlation between the Fe^{+3} content of chlorite and temperature, and that only at T<250°C the $Fe^{+3}/\Sigma Fe$ ratio of chlorite is higher than 0.10. We are therefore confident that, at the temperatures considered in the modelling (T>400°C), the influence of Fe^{+3} in chlorite may be neglected.

DISCUSSION
The *P–T* evolution of the Basal Serpentinite Unit
The exceptionally well preserved prograde assemblage of the studied FeTi-oxide eclogite-facies metagabbro allowed us to reconstruct in detail a segment of the Basal Serpentinite Unit prograde evolution, from about 420°C, 16 kbar to peak conditions of ≥550°C, 25-26 kbar (Fig. 6). The first stages of evolution (i.e. growth of Grt_{1a-1c}) should be considered with care, because a number of problems could induce uncertainties on the reliability of the constrained *P–T* conditions (see the above discussion). The estimated peak conditions are very similar to that obtained by Messiga *et al.* (1999) for a chloritoid + talc-bearing metagabbro from the Lago Superiore Unit, structurally upward in the Monviso metaophiolites, whereas *P* estimates are considerably higher than those proposed by Blake *et al.* (1995) for the same Basal Serpentinite Unit. However, pressures obtained by Blake *et al.* (1995) were only minimum pressures, because they were based on the Jd-in-omphacite barometer.

Previous authors did not report *P–T* constraints for the prograde stages of metamorphism in the Monviso metaophiolites: thus, in this paper we propose the first reconstruction of the prograde evolution for a Monviso unit. Our data show that subduction occurred along very low thermal gradients, typical of cold subduction zones and compatible with the lawsonite formation (e.g. Liou *et al.*, 2004). More in detail, it is evident that the thermal gradient changed through time during subduction, decreasing from about 9°C/km to less than 7°C/km (assuming an average density of 3.0 g/cm^3) (Fig. 6). A similar decrease of the thermal gradient in the oceanic Piedmonte Zone subducting slab has been described in the Zermatt-Saas Zone of Western Alps for the ultra-high pressure Lago di Cignana Unit and its adjoining units (Groppo *et al.*, 2009a), and interpreted as the evidence of a progressive increase in the subduction rate. This interpretation is consistent with observations and models that require a significant length of slab to be present at mantle depth to act as an engine for subduction (Royden & Husson, 2006).

The lawsonite breakdown during subduction and the devolatilization reactions

The data presented in this paper show that eclogitization of the studied metagabbro was accompanied by a significant prograde loss of fluids, mainly related to the breakdown of lawsonite and chlorite. This conclusion is in line with the results of Philippot & Selverstone (1991) and Nadeau *et al.* (1993) on similar rocks from the same area (Lago Superiore Unit, directly overlying the Basal Serpentinite Unit). However, the new *P–T* constraints provided by the pseudosection modelling allow us to conclude that most of these fluids were released at a depth of about 65-70 km, a considerably higher depth than that estimated by these Authors (ca. 40 km). Our results are also in line with those of Lü *et al.* (2009) which recognized two critical dehydration processes (related to the breakdown of chlorite and glaucophane + lawsonite, respectively) during subduction of UHP coesite-bearing eclogites from Tianshan.

Reactions responsible for the lawsonite breakdown have been experimentally investigated for both basaltic and andesitic compositions (Poli & Schmidt, 1995; Okamoto & Maruyama, 1999). Experimental results suggest that, at pressures higher than the zoisite/clinozoisite stability field, the destabilization of lawsonite results in assemblages composed of anhydrous minerals, i.e. in garnet + clinopyroxene + quartz/coesite ± kyanite (Poli & Schmidt, 1995; Okamoto & Maruyama, 1999). Lawsonite disappearance in the basaltic system at H_2O saturated conditions is ascribed to a continuous reaction of the type: $Lws + Cpx + Grt_1 = Grt_2 + Qtz/Coe + H_2O$ (reaction 2 of Poli & Schmidt, 1995), where garnet progressively shifts toward grossular-rich compositions along a prograde P–T path (Okamoto & Maruyama, 1999; Poli *et al.*, 2009).

The studied FeTi-oxide metagabbro OF2727 has a bulk composition that differs from a common basaltic composition, being significantly enriched in both Fe and Ti ($FeO_{tot} \approx 21$ wt%, $TiO_2 \approx 5.5$ wt%). Therefore, different reactions controlling the lawsonite breakdown are expected. Microstructural and mineral chemical observations suggest that both garnet and omphacite compositions significantly changed during lawsonite breakdown (i.e. $Grt_{1 \to 2}$ and $Omp_{2 \to 3}$ transition coincides with the disappearance of lawsonite, see Table 3). However, contrary to the experimental data of Poli & Schmidt (1995), Okamoto & Maruyama (1999) and Poli *et al.* (2009), the grossular content of garnet sharply decreases simultaneously with the lawsonite disappearance. The dehydration reactions modelled for the metagabbro composition (i.e. equilibria A1-A9 and B1-B4 of Fig. 8) suggest that: (i) quartz is always a reactant (whereas it is a product in the reactions proposed by Poli & Schmidt, 1995 and Okamoto & Maruyama, 1999), and (ii) chemical re-

equilibration of omphacite (and not of garnet) is involved in the dehydration process. In particular, omphacite becomes enriched in the diopsidic component (Fig. 8) up-temperatures, thus suggesting that Ca released from lawsonite is exchanged with clinopyroxene instead of garnet. Therefore, comparing our results with experimental data, we suggest that the bulk composition of the system could have a strong influence on the dehydration reactions occurring during subduction.

Changing redox state of FeTi-oxide metagabbro during subduction
Our modelling also suggests that dehydration equilibria involved in the lawsonite and chlorite breakdown also release O_2, thus controlling the redox state of the system during subduction (Fig. 9). This result has interesting implications for the understanding of the complex interactions between crust and mantle in the subduction zones. The slab-derived fluid phases, in fact, have been suggested as the agents for the oxidized nature of the mantle wedge compared to the oceanic mantle, as evidenced by: (i) strongly-oxidized xenoliths coming from subduction-related areas (Wood *et al.*, 1990; Carmichael, 1991; Ballhaus, 1993; Parkinson & Arculus, 1999; Peslier *et al.*, 2002) and (ii) oxygen fugacity data from orogenic peridotites (Malaspina *et al.*, 2009). Although it is accepted that the mantle wedge above subduction zones is oxidized, the exact processes of relative oxidation are still controversial (e.g. Parkinson & Arculus, 1999; Malaspina *et al.*, 2009; Rowe *et al.*, 2009). However, it is widely recognized that oxidized components are transferred to the overlying mantle wedge by fluids and/or melts coming from the subducting slab (e.g. Parkinson & Arculus, 1999; Peslier *et al.*, 2002; Malaspina *et al.*, 2009; Rowe *et al.*, 2009). H_2O-rich fluids have been alternatively interpreted as very effective oxidizing agents (Brandon & Draper, 1996, 1998) or as extremely poor oxidizing agents (Ballhaus, 1993; Frost & Ballhaus, 1998). According to the first hypothesis (Brandon & Draper, 1996), water may be an oxidizing agent because, after dissociation, oxygen forms ferric iron and hydrogen escapes the system. Conversely, Frost & Ballhaus (1998) argued that the very low H_2O dissociation constant hampers its oxidizing capability. According to our data, the oxidation of the mantle wedge may be triggered by dehydration–redox reactions that occur, at least locally, in the subducting slab. This hypothesis must be considered as preliminary, since FeTi-oxide metagabbros are minor components of the subducting slab. However, our results represent a contribution to clarify if and how the metamorphic transformations occurring in the subducting slab play a role in the oxidation of the overlying mantle wedge.

Published Fe^{+3} data on omphacite in other Fe-Ti oxide metagabbros from the Western Alps (Pognante, 1985; Pognante & Kienast, 1987) also show prograde omphacite enriched in Fe^{+3} with respect to peak omphacite, thus suggesting, at least for this kind of protolith, the existence of a correlation between decreasing Fe^{+3} in omphacite and increasing metamorphic grade. Further and complementary work on other representative lithologies (metabasalts and MgAl-metagabbros) from similar palaeosubduction zones is needed to generalize this result to the whole subducting slab.

Appendix A. Analytical methods

Mineral chemistry

The rock-forming minerals were analysed with both Scanning Electron Microscope (SEM)-Energy-Dispersive Spectrometer (EDS) and Electron-MicroProbe Analyser (EMPA) – Wavelength-Dispersion Spectrometer (WDS). A Cambridge Stereoscan 360 SEM equipped with an EDS Energy 200 and a Pentafet detector (Oxford Instruments) was used at the Department of Mineralogical and Petrological Sciences, University of Torino (Italy) with the following operating conditions: 50 seconds counting time and 15 kV accelerating voltage. SEM-EDS quantitative data (spot size = 2 μm) were acquired and processed using the Microanalysis Suite Issue 12, INCA Suite version 4.01; the raw data were calibrated on natural mineral standards and the ΦρZ correction (Pouchou & Pichoir, 1988) was applied. Qualitative EDS elemental maps of Fig. 3 were acquired using 15 kV accelerating potential, a very short dwell time of 120 ms (corresponding to an acquisition time of ca. 12 hours, including a detector dead time ca. 30%) and at a resolution of 512 × 512 pixels. A JEOL 8200 Superprobe (WDS) was used at the Department of Earth Sciences, University of Milano (Italy). Acceleration voltage was set to 15 kV, beam current was 15 nA and natural minerals were used as standards. A ΦρZ routine was used for matrix correction.

$Fe^{+3}/\Sigma Fe$ estimate in garnet and omphacite

The $Fe^{+3}/\Sigma Fe$ ratio of garnet was measured by electron microprobe with the "flank method" (Höfer *et al.*, 1994; Höfer & Brey, 2007) calibrated on the JEOL 8200 Superprobe at the Department of Earth Sciences, University of Milano (Malaspina *et al.*, 2009). Combined "flank method" and quantitative elemental analysis were performed on wavelength-dispersive spectra (WDS) at 15 kV and 60 nA. One spectrometer with a TAP crystal and 300 μm slit was used for the "flank method", measuring the FeLβ and FeLα at counting time of 300 s (Fig. SM3c, available as Supplementary Material). With the remaining 4 spectrometers Si, Ti, Al, Cr, Fe, Mg, Mn and Ca were measured simultaneously. The quantitative $Fe^{+3}/\Sigma Fe$ in garnets was determined by applying the correction for self-absorption (see Höfer & Brey, 2007 for details), using natural and synthetic garnet end-members with fixed $Fe^{+3}/\Sigma Fe$ as standards (Malaspina *et al.* 2009). Mineral analyses were always performed using detailed back-scattered electron images to check the microtextural site. The accuracy of the "flank method" has been demonstrated in previous studies, where an error between ±0.02 and ±0.04 for $Fe^{+3}/\Sigma Fe$ has been documented in samples with 8-11 wt% total Fe (Höfer & Brey, 2007).

The $Fe^{+3}/\Sigma Fe$ ratios of pyroxenes were calculated assuming stoichiometry and 4 cations based on 6 oxygen atoms, and the classification of Morimoto *et al.*, (1988) was used. The calculated $Fe^{+3}/\Sigma Fe$ ratios do not change using the method of Matsumoto & Hirajima (2005), which considers $Fe^{+3} = Na - {}^{VI}Al_{Jd}$ [for Si>2.00, ${}^{VI}Al_{Jd} = Al_{tot}$; for Si<2.00, ${}^{VI}Al_{Jd} = Al_{tot} - 2{}^{IV}Al$ and ${}^{IV}Al = 2 - Si$].

Bulk-composition calculation by combining mineral modes and compositions

Qualitative major elements X-ray maps of a representative portion of the thin section (ca. 8 × 6 mm) have been acquired using a μ-XRF Eagle III-XPL spectrometer equipped with an EDS Si(Li) detector and with an Edax Vision32 microanalytical system, located at the Department of Mineralogical and Petrological Sciences, University of Torino. The operating conditions were: 400 ms counting time, 40 kV accelerating voltage and a probe current of 800 μA. A spatial resolution of about 30 μm in both x and y directions has been used; the spot size is ca. 30 μm. Quantitative modal

amounts of each mineral phase have been obtained by processing the μ-XRF maps with the software program Petromod (Cossio *et al.*, 2000) (Fig. SM2, available as Supplementary Material). The bulk-rock composition of sample OF2727 has been then calculated by combining the mineral proportions obtained from the modal estimate of the micro-XRF maps with mineral chemistry acquired at SEM-EDS (Table SM1, available as Supplementary Material).

Appendix B. Details on the pseudosections calculation
The evolution of metagabbro OF2727 has been modelled in the system MnNCFMASTHO. Fluid phase, assumed to be pure H_2O, was considered in excess because water saturation is essential to consider the lawsonite stability (Clarke *et al.*, 2006). K_2O was not considered in the calculation because of its very low content in the bulk composition.
Pseudosections have been calculated following the approach of Connolly (1990, 2009) (Perple_X version 08) and using the internally consistent thermodynamic dataset and equation of state for H_2O of Holland & Powell (1998, revised 2004). The minerals considered in the calculation were: garnet, omphacite, chlorite, amphibole, lawsonite, talc, epidote, paragonite, quartz, rutile, ilmenite, titanite and magnetite. The following solid-solution models were used: garnet and epidote (Holland & Powell, 1998), omphacite (Green *et al.*, 2007), chlorite (Holland *et al.*, 1998), amphibole (Diener *et al.*, 2007), plagioclase (Newton *et al.*, 1980) and talc (ideal model). Pumpellyite has not been considered in the calculation because its stability is limited to $T < 350°C$ and $P < 8$ kbar (e.g. Rossetti & Ferrero, 2008), i.e. at $P–T$ conditions not considered in the modelling.

Appendix C. Details on the calculations of dehydration and redox reactions
The dehydration equilibria occurring within the quini-variant field Lws+Qtz+Chl+Omp+Grt+Rt of pseudosection reported in Fig. 5b have been re-calculated (Fig. 8) for composition 1e in the system NCFMASTHO and using the same solution models of Fig. 5. In this case, however, spessartine and amesite end-members have not been included in the solution models, due to the very low content of these end-members in garnet and chlorite, respectively. This approximation is also required because the new pseudosection of Fig. 8 is the starting point for the modelling of the redox equilibria in the T-log$f(O_2)$ projection of Fig. 9 and an exact correspondence between the two grids is needed. Simplification of the solid-solutions in the modelling of redox equilibria reduces the number of pseudocompounds (and thus the number of the calculated equilibria) and avoids numerical overflow. As a consequence of this simplification, the garnet-in and lawsonite-out curves are shifted up-T and down-T of 20°C and 15°C, respectively, at constant P (compare Fig. 5b and Fig. 8).

Appendix D. Supplementary Material
Supplementary data include: (i) representative microstructure of the studied sample OF2727 compared with those of two other FeTi-oxide metagabbros from the same area (Fig. SM1); (ii) the processed μ-XRF map used for the modal estimate of the phase proportions (Fig. SM2); (iii) additional compositional profiles for garnet and information from the flank method used to estimate the $Fe^{+3}/\Sigma Fe$ ratio (Fig. SM3); (iv) the comparison between the bulk composition of sample OF2727 and other metagabbros from the Western Alps (Fig. SM4); (v) some details on the method used to calculate the effects of chemical fractionation on the bulk composition due to the growth of zoned garnet (Fig. SM5); (vi) a set of $P–T$ pseudosections for stages I and II (1a, 1e, 2a and 2c) with compositional isopleths of garnet and omphacite, calculated at different XFe_2O_3 values and used for the XFe_2O_3 estimate (Fig. SM6a, b); (vii) the complete set of $P–T$ pseudosections for stages I and II

(1a-1e, 2a-2c), calculated at $XFe_2O_3 = 0.20$ and 0.15 respectively, with compositional isopleths of garnet and omphacite (Fig. SM7a-d); (viii) a table, showing the bulk composition of sample OF2727 estimated from mineral modes and compositions (Table SM1).

REFERENCES

Ballhaus, C. (1993). Oxidation states of the lithospheric and asthenospheric upper mantle. *Contribution to Mineralogy and Petrology* **114**, 331–348.

Blake, C., Moore, D.G. & Jayko, A.S. (1995). The role of the serpentinite melange in the unroofing of the UHP rocks: an example from the western Alps in Italy. In: Coleman, R.G. & Wang, X. (eds) *Ultrahigh pressure metamorphism*. Cambridge University Press, 182–205.

Bocchio, R., Benciolini, L., Martin, S. & Tartarotti P. (2000). Geochemistry of eclogitised Fe-Ti gabbros from various lithological settings (Aosta Valley ophiolites, Italian western Alps). Protolith composition and eclogitic paragenesis. *Periodico di Mineralogia* **69**, 217–237.

Brandon, A.D. & Draper, D.S. (1996). Constraints on the origin of the oxidation state of mantle overlying subduction zones: an example from Simcoe, Washington, USA. *Geochimica and Cosmochimica Acta* **60**, 1739–1749.

Brandon, A.D. & Draper, D.S. (1998). Reply to the comment by B.R. Frost and C. Ballhaus on "Constraints on the origin of the oxidation state of mantle overlying subduction zones: an example from Simcoe, Washington, USA". *Geochimica and Cosmochimica Acta* **62**, 333–335.

Bucher, M. & Frey, K. (2002). *Petrogenesis of metamorphic rocks*. Springer-Verlag, 7th edition, Berlin, 341 p.

Carmichael, I.S.E. (1991). The oxidation state of basic magmas: a reflection of their source regions? *Contribution to Mineralogy and Petrology* **106**, 129–142.

Carson, C.J., Powell, R. & Clarke, G.L. (1999). Calculated mineral equilibria for eclogites in CaO-Na$_2$O-FeO-MgO-Al$_2$O$_3$-SiO$_2$-H$_2$O: application to the Pouebo Terrane, Pam Peninsula, New Caledonia. *Journal of Metamorphic Geology* **17**, 9–24.

Castelli, D. & Lombardo, B. (2007). The plagiogranite - FeTi-oxide gabbro association of Vernè (Monviso metamorphic ophiolite, Western Alps). *Ofioliti* **32**, 1–14.

Castelli, D., Rostagno, C. & Lombardo, B. (2002). Jd-Qtz-bearing metaplagiogranite from the Monviso meta-ophiolite (Western Alps). *Ofioliti* **27**, 81–90.

Clarke, G.L., Aitchison, J.C. & Cluzel, D. (1997). Eclogites and blueschists of the Pam Peninsula, NE New Caledonia: a reappraisal. *Journal of Petrology* **38**, 843–876.

Clarke, G.L., Powell, R. & Fitzherbert, J. (2006). The lawsonite paradox: a comparison of field evidence and mineral equilibria modelling. *Journal of Metamorphic Geology* **24**, 715–725.

Clift, P.D., Rose, E.F., Shimizu, N., Layne, G.D., Draut, A.E. & Regelous, M. (2001). Tracing the evolving flux from the subducting plate in the Tonga–Kermadec arc system using boron in volcanic glass. *Geochimica and Cosmochimica Acta* **65**, 3347– 3364.

Connolly, J.A.D. (1990). Multivariable phase diagrams: an algorithm based on generalized thermodynamics. *American Journal of Science* **290**, 666–718.

Connolly, J.A.D. (2009). The geodynamic equation of state: what and how. G*eochemistry, Geophysics, Geosystems* **10**, Q10014.

Connolly, J.A.D. & Kerrick, D.M., 1987. An algorithm and computer program for calculating computer phase diagrams. *CALPHAD* **11**, 1–55.

Cossio, R., Borghi, A. & Ruffini, R. (2002). Quantitative modal determination of geological samples based on X-ray multielemental map acquisition. *Microscopy and Microanalysis* **8**, 139–149.

Dasgupta, R. & Hirschmann, M.M. (2006). Melting in the Earth's deep upper mantle caused by carbon dioxide. *Nature* **440**, 659–662.

Dasgupta, R., Hirschmann, M.M. & Withers, A.C. (2004). Deep global cycling of carbon constrained by the solidus of anhydrous, carbonated eclogite under upper mantle conditions. *Earth and Planetary Science Letters* **227**, 73–85.

Davis, P.B. & Whitney, D.L. (2006). Petrogenesis of lawsonite and epidote eclogite and blueschist, Sivrihisar Massif, Turkey. *Journal of Metamorphic Geology* **24**, 823–849.

Davis, P.B. & Whitney, D.L. (2008). Petrogenesis and structural petrology of high pressure metabasalt pods, Sivrihisar, Turkey. *Contribution to Mineralogy and Petrology* **156**, 217–241.

Diener, J.F.A., Powell, R., White, R.W. & Holland, T.J.B. (2007). A new thermodynamic model for clino- and orthoamphiboles in the system Na_2O–CaO–FeO–MgO–Al_2O_3–SiO_2– H_2O–O. *Journal of Metamorphic Geology* **25**, 631–656.

Evans, T.P. (2004). A method for calculating effective bulk composition modification due to crystal fractionation in garnet-bearing schist: implication for isopleth thermobarometry. *Journal of Metamorphic Geology* **22**, 547–557.

Forneris, J.F. & Holloway, J.R. (2003). Phase equilibria in subducting basaltic crust: implications for H_2O release from the slab. *Earth and Planetary Science Letters* **214**, 187–201.

Frost, B.R. & Ballhaus, C. (1998). Comment on "Constraints on the origin of the oxidation state of mantle overlying subduction zones: an example from Simcoe, Washington, USA". *Geochimica and Cosmochimica Acta* **62**, 329–331.

Gaidies, F., Abart, R., De Capitani, C., Schuster, R., Connolly, J.A.D. & Reusser, E. (2006). Characterization of polymetamorphism in the Austroalpine basement east of the Tauern Window using garnet isopleth thermobarometry. *Journal of Metamorphic Geology* **24**, 451–475.

Ghent, E., Tinkham D. & Marr R. (2009). Lawsonite eclogites from the Pinchi Lake area, British Columbia: new P–T estimates and interpretation. *Lithos* **109**, 248–253.

Green, E.C.R., Holland, T.J.B. & Powell, R. (2007). An order-disorder model for omphacitic pyroxenes in the system jadeite–diopside–hedenbergite–acmite, with applications to eclogitic rocks. *American Mineralogist* **92**, 1181–1189.

Groppo, C., Beltrando, M. & Compagnoni, R. (2009a). *P–T* path of the UHP Lago di Cignana and adjoining HP meta-ophiolitic units: insights into the evolution of subducting tethyan slab. *Journal of Metamorphic Geology* **27**, 207–231.

Groppo, C., Forster, M., Lister, G. & Compagnoni, R. (2009b). Glaucophane schist and associated rocks from Sifnos (Cyclades, Greece): new constraints on the *P–T* evolution from oxidized systems. *Lithos* **109**, 254–273.

Groppo, C., Lombardo, B., Castelli, D. & Compagnoni, R. (2007). Exhumation history of the UHPM Brossasco-Isasca Unit, Dora-Maira Massif, as inferred from a phengite-amphibole eclogite. *International Geology Review* **49**, 142–168.

Groppo, C. & Rolfo, F. (2008). *P–T* evolution of the Aghil Range between Kunlun and Karakorum (SW Sinkiang, China). *Lithos* **105**, 365–378.

Hacker, B.R., Abers, G.A. & Peacock, S.M. (2003). Subduction factory: 1. Theoretical mineralogy, densities, seismic wave speeds, and H_2O contents. *Journal of Geophysical Research* **108**, ESE 10/1–10/26.

Hawkesworth, C.J., Gallagher, K., Hergt, J.M. & McDermott, F. (1993). Mantle and slab contributions in arc magmas. *Annual Review of Earth and Planetary Sciences* **21**, 175–204.

Höfer, H.E. & Brey, G.P. (2007). The iron oxidation state of garnet by electron microprobe: its determination with the flank method combined with major-element analysis. *American Mineralogist* **92**, 873–885.

Höfer, H.E., Bry, G.P., Schulz-Dobrick, B. & Oberhänsli, R. (1994). The determination of the oxidation state of iron by the electron microprobe. *European Journal of Mineralogy* **6**, 407–418.

Holland, T., Baker, J. & Powell, R. (1998). Mixing properties and activity-composition relationships of chlorites in the system MgO-FeO- Al_2O_3-SiO_2- H_2O. *European Journal of Mineralogy* **10**, 395–406.

Holland, T.J.B. & Powell, R. (1998). An internally consistent thermodynamic data set for phases of petrologic interest. *Journal of Metamorphic Geology* **16**, 309–343.

Kerrick, D.M. & Connolly, J.A.D. (1998). Subduction of ophicarbonates and recycling of CO_2 and H_2O. *Geology* **26**, 375–378.

Kerrick, D.M. & Connolly, J.A.D. (2001a). Metamorphic devolatilization of subducted marine sediments and the transport of volatiles into the Earth's mantle. *Nature* **411**, 293–295.

Kerrick, D.M. & Connolly, J.A.D. (2001b). Metamorphic devolatilization of subducted oceanic metabasalts: implications for seismicity, arc magmatism and volatile recycling. *Earth and Planetary Science Letters* **189**, 19–29.

Korzhinskii, D.S. (1959). Physicochemical basis of the analysis of the paragenesis of minerals. Consultants Bureau, New York, 19 p.

Lagabrielle, Y. & Lemoine, M. (1997). Alpine, Corsican and Apennine ophiolites: the slow-spreading ridge model. *Comptes Rendus de l'Académie des Sciences - Series IIA - Earth and Planetary Science* **325**, 909–920.

Leake, B.E., Woolley, A.R., Arps, C.E.S., Birch, W.D. *et al.* (1997). Nomenclature of amphiboles: Report of the Subcommittee on Amphiboles of the International Mineralogical Association, Commission on New Minerals and Mineral Names. *American Mineralogist* **82**, 1019–1037.

Liou, J.G., Tsujimori, T., Zhang, R.Y., Katayama, I., & Maruyama, S. (2004). Global UHP metamorphism and continental subduction/collision: The Himalayan model. *International Geology Review*, **46**, 1−27.

Liu, J., Bohlen, S.R. & Ernst, W.G. (1996). Stability of hydrous phases in subducting oceanic crust. *Earth and Planetary Science Letters* **143**, 161–171.

Lombardo, B., Nervo, R., Compagnoni, R., Messiga, B., Kienast, J.R., Mével, C., Fiora, L., Piccardo, G.B. & Lanza, R. (1978). Osservazioni preliminari sulle ofioliti metamorfiche del Monviso (Alpi Occidentali). *Rendiconti della Società Italiana di Mineralogia e Petrologia* **34**, 253–305.

Lombardo, B., Rubatto, D. & Castelli, D. (2002). Ion microprobe U-Pb dating of zircon from a Monviso metaplagiogranite: Implications for the evolution of the Piedmont-Liguria Tethys in the Western Alps. *Ofioliti* **27**, 109–117.

Lü, Z., Zhang, L., Du, J. & Bucher, K. (2009). Petrology of coesite-bearing eclogite from Habutengsu Valley, western Tianshan, NW China and ist tectonometamorphic implication. *Journal of Metamorphic Geology* **27**, 773–787.

Malaspina, N., Poli, S. & Fumagalli P. (2009). The oxidation state of metasomatized mantle wedge: insights from C-O-H-bearing garnet peridotite. *Journal of Petrology* **50**, 1533–1552.

Marmo, B.A., Clarke, G.L. & Powell, R. (2002). Fractionation of bulk rock composition due to porphyroblast growth; effects on eclogite facies mineral equilibria, Pam Peninsula, New Caledonia. *Journal of Metamorphic Geology* **20**, 151–165.

Matsumoto, K. & Hirajima, T. (2005). The coexistence of jadeite and omphacite in an eclogite-facies metaquartz diorite from the southern Sesia Zone, Western Alps, Italy. *Journal of Mineralogical and Petrological Sciences* **100**, 70–84.

Messiga, B., Kienast, J.R., Rebay, G., Riccardi, M.P., Tribuzio, R. (1999). Cr-rich magnesiochloritoid eclogite from the Monviso ophiolites (Western Alps, Italy). *Journal of Metamorphic Geology* **17**, 287–299.

Miyazoe, T., Nishiyama, T., Uyeta, K., Miyazaki, K. & Mori, Y. (2009). Coexistence of pyroxenes jadeite, omphacite, and diopside/hedembergite in an albite-omphacite rock from a serpentinite mélange in the Kurosegawa Zone of Central Kyushu, Japan. *American Mineralogist* **94**, 34–40.

Molina, J.F. & Poli, S. (2000). Carbonate stability and fluid composition in subducted oceanic crust: an experimental study on H_2O–CO_2-bearing basalts. *Earth and Planetary Science Letters* **176**, 295–310.

Morimoto, N., Fabries, J., Ferguson, A.K., Ginzburg, I.V., Ross, M., Seifert, F.A., Zussman, J., Aoki, K. & Gottardi, G. (1988). Nomenclature of pyroxenes. *American Mineralogist* **73**, 1123−1133

Nadeau, S., Philippot, P. & Pineau, F. (1993). Fluid inclusion and mineral isotopic compositions (H-C-O) in eclogitic rocks as tracers of local fluid migration during high-pressure metamorphism. *Earth and Planetary Science Letters* **114**, 431–448.

Newton, R.C., Charlu, T.V. & Kleppa, O.J. (1980). Thermochemistry of the high structural state plagioclases. *Geochimica and Cosmochimica Acta* **44**, 933–941.

Okamoto, K. & Maruyama, S. (1999). The high-pressure synthesis of lawsonite in the MORB + H_2O system. *American Mineralogist* **84**, 362–373.

Parkinson, I.J. & Arculus, R.J. (1999). The redox state of subduction zones: insights from arc peridotites. *Chemical Geology* **160**, 409–423.

Pawley, A.R. & Holloway, J.R. (1993). Water sources for subduction zone volcanism; new experimental constraints. *Science* **260**, 664– 667.

Peacock, S.M. (1993). The importance of blueschist-eclogite dehydration reactions in subducting oceanic crust. *Geological Society of America Bulletin* **105**, 684– 694.

Peacock, S.M. & Wang, K. (1999). Seismic consequences of warm versus cool subduction zone metamorphism: Examples from northeast and southwest Japan. *Science* 286, 937–939.

Peslier, A.H., Luhr, J.F. & Post, J. (2002). Low water contents in pyroxenes from spinel-peridotites of the oxidized, sub-arc mantle wedge. *Earth and Planetary Science Letters* **201**, 69–86.

Philippot, P. & Selverstone, J. (1991). Trace-element-rich brines in eclogitic veins: implications for fluid composition and transport during subduction. *Contribution to Mineralogy and Petrology* **106**, 417–430.

Philippot, P. (1988). Déformation et éclogitisation progressives d'une croûte océanique subductée (Le Monviso, Alpes occidentales) : contraintes cinématiques durant la collision alpine. Thèse univ. Montpellier, 269 p.

Pognante, U. (1985). Coronitic reactions and ductile shear zones in eclogitized ophiolite metagabbro, western Alps, north Italy. *Chemical Geology* **50**, 99–109.

Pognante, U., Lombardo, B. & Venturelli, G. (1982). Petrology and geochemistry of Fe-Ti gabbros and plagiogranites from the Western Alps Ophiolites. *Schweizer Mineralogische und Petrographische Mitteilungen* **62**, 457–472.

Pognante, U. & Kienast, J.-R. (1987). Blueschist and eclogite transformations in Fe-Ti gabbros: a case from the western Alps ophiolites. *Journal of Petrology* **28**, 271–292.

Pognante, U. & Toscani, L. (1985). Geochemistry of basaltic and gabbroid metaophiolites from the Susa Valley, Italian Western Alps. *Schweizer Mineralogische und Petrographische Mitteilungen* **65**, 265–277.

Poli, S., Franzolin, E., Fumagalli, P. & Crottini, A. (2009). The transport of carbon and hydrogen in subducted oceanic crust: an experimental study to 5 GPa. *Earth and Planetary Science Letters* **278**, 350–360.

Poli, S. & Schmidt, M.W. (1995). H_2O transport and release in subduction zones —experimental constraints on Basaltic and Andesitic Systems. *Journal of Geophysical Research* 100, 22299–22314.

Pouchou, J.L. & Pichoir, F. (1988). Determination of mass absorption coefficients for soft X-Rays by use of the electron microprobe. Microbeam Analysis, San Francisco Press, 319–324.

Powell, R. & Holland, T.J.B. (2008). On thermobarometry. *Journal of Metamorphic Geology* **26**, 155–179.

Proyer, A., Dachs, E. & McCammon, C. (2004). Pitfalls in geothermobarometry of eclogites: Fe^{3+} and changes in the mineral chemistry of omphacite at ultrahigh pressures. *Contribution to Mineralogy and Petrology* **147**, 305–318.

Rossetti, P. & Ferrero, S. (2008). The Zn-Pb deposits of Casario (Ligurian Alps, NW Italy): late Palaeozoic sedimentary-exhalative bodies affected by the alpine metamorphism. *Geodinamica Acta* **21**, 117–137.

Rowe, M.C., Kent, A.J.R. & Nielsen, R.L. (2009). Subduction influence on oxygen fugacity and trace and volatile elements in basalts across the Cascade Volcanic Arc. *Journal of Petrology* **50**, 61–91.

Royden, L.H. & Husson, L. (2006). Trench motion, slab geometry and viscous stresses in subduction systems. *Geophysical Journal International* **167**, 881–905.

Rubatto, D. & Hermann, J. (2003). Zircon formation during fluid circulation in eclogites (Monviso Western Alps): implications for Zr and Hf budget in subduction zones. *Geochimica and Cosmochimica Acta* **67**, 2173–2187.

Rüpke, L.H., Morgan, J.P., Hort, M. & Connolly, J.A.D. (2004). Serpentine and the subduction zone water cycle. *Earth and Planetary Science Letters* **223**, 17–34.

Schellart, W.P., Freeman, J., Stegman, D.R., Moresi, L. & May, D. (2007). Evolution and diversity of subduction zones controlled by slab width. *Nature* 446, 308–311.

Schmid, R., Wilke, M., Oberhänsli, R., Janssens, K., Falkenberg, G., Franz, L. & Gaab, A. (2003). Micro-XANES determination of ferric iron and its application in thermobarometry. *Lithos* **70**, 381–392.

Schmidt, M.W. & Poli, S. (1998). Experimentally based water budgets for dehydrating slabs and consequences for arc magma generation. *Earth and Planetary Science Letters* **163**, 361–379.

Schwartz, S., Lardeaux, J-M., Guillot, S. & Tricart, P. (2000). Diversité du métamorphisme éclogitique dans le massif ophiolitique du Monviso (Alpes occidentales, Italie). *Geodinamica Acta* **13**, 169–188.

Sobolev, V.N., McCammon, C.A., Taylor, L.A., Snyder, G.A. & Sobolev, N.V. (1999). Precise Mössbauer milliprobe determination of ferric iron in rock-forming minerals and limitations of electron microprobe analysis. *American Mineralogist* **84**, 78–85.

Spandler, C., Hermann, J., Arculus, R. & Mavrogenes, J. (2004). Geochemical heterogeneity and element mobility in deeply subducted oceanic crust: insights from high pressure mafic rocks from New Caledonia. *Chemical Geology* **206**, 21–42.

Štîpská, P. & Powell, R. (2005). Constraining the *P–T* path of a MORB-type eclogite using pseudosections, garnet zoning and garnet-clinopyroxene thermometry: an example from the Bohemian Massif. *Journal of Metamorphic Geology* **23**, 725–743.

Stüwe, K. (1997). Effective bulk composition changes due to cooling: a model predicting complexities in retrograde reaction textures. *Contribution to Mineralogy and Petrology* **129**, 43–52.

Tsujimori, T., Liou. J.G. & Coleman, R.G. (2005). Coexisting retrograde jadeite and omphacite in a jadeite-bearing lawsonite eclogite from the Montagua Fault Zone, Guatemale. *American Mineralogist* **90**, 836–842.

Tsujimori, T., Sisson, V.B., Liou, J.G., Harlow, G.E. & Sorensen, S.S. (2006a). Petrologic characterization of Guatemalan lawsonite-eclogite: eclogitization of subducted oceanic crust in a cold subduction zone. In: Hacker, B.H., McClelland, W.C. & Liou, J.G.(eds.) *Ultrahigh-pressure metamorphism: deep continental subduction*. GSA Special Paper **403**, 127–138.

Tsujimori, T., Sisson, V.B., Liou, J.G., Harlow, G.E. & Sorensen, S.S. (2006b). Very-low-temperature record of the subduction process: a review of worldwide lawsonite eclogites. *Lithos* 92, 609–624.

Vidal, O., De Andrade, V., Lewin, E., Munoz, M., Parra, T. & Pascarelli, S. (2006). *P–T*-deformation-Fe^{3+}/Fe^{2+} mapping at the thin section scale and comparison with XANES mapping: application to a garnet-bearing metapelite from the Sambagawa metamorphic belt (Japan). *Journal of Metamorphic Geology* **24**, 669–683.

Warren, C.J. & Waters, D.J. (2006). Oxidized eclogites and garnet-blueschists from Oman: *P–T* path modelling in the NCFMASHO system. *Journal of Metamorphic Geology* **24**, 783–802.

Wei, C.J., Powell, R. & Zhang, L.F. (2003). Eclogite from the southern Tianshan, NW China: petrological characteristic and calculated mineral equilibria in the Na_2O-CaO-FeO-MgO- Al_2O_3-SiO_2- H_2O system. *Journal of Metamorphic Geology* **21**, 163–179.

Wei, C.J., Yang, Y., Su, L., Song, S.G. & Zhang, L.F. (2009). Metamorphic evolution of low-*T* eclogite from the North Qilian orogen, NW China: evidence from petrology and calculated phase equilibria in the system NCKFMASHO. *Journal of Metamorphic Geology* **27**, 55–70.

White, R.W., Powell, R. & Holland, T.J.B. (2007). Progress relating to calculation of partial melting equilibria for metapelites. *Journal of Metamorphic Geology* **25**, 511–527.

Will, T.M., Okrusch, M., Schmädicke, E. & Chen, G. (1998). Phase relations in the greenschist-blueschist-amphibolite-eclogite facies in the system Na_2O-CaO-FeO-MgO- Al_2O_3-SiO_2- H_2O (NCFMASH), with applications to the *PT*-evolution of metamorphic rocks from Samos, Greece. *Contribution to Mineralogy and Petrology* **32**, 85–102.

Wood, B.J., Bryndzia, L.T. & Johnson, K.E. (1990). Mantle oxidation state and its relationship to tectonic environment and fluid speciation. *Science* 248, 337–345.

Yaxley, G.M. & Green, D.H. (1994). Experimental demonstration of refractory carbonate bearing eclogite and siliceous melt in the subduction regime. *Earth and Planetary Science Letters* **128**, 313–325.

Zuluaga, C.A., Stowell, H. & Tinkham, D. (2005). The effect of zoned garnet on metapelite pseudosection topology and calculated metamorphic *P–T* paths. *American Mineralogist* **90**, 1619–1628.
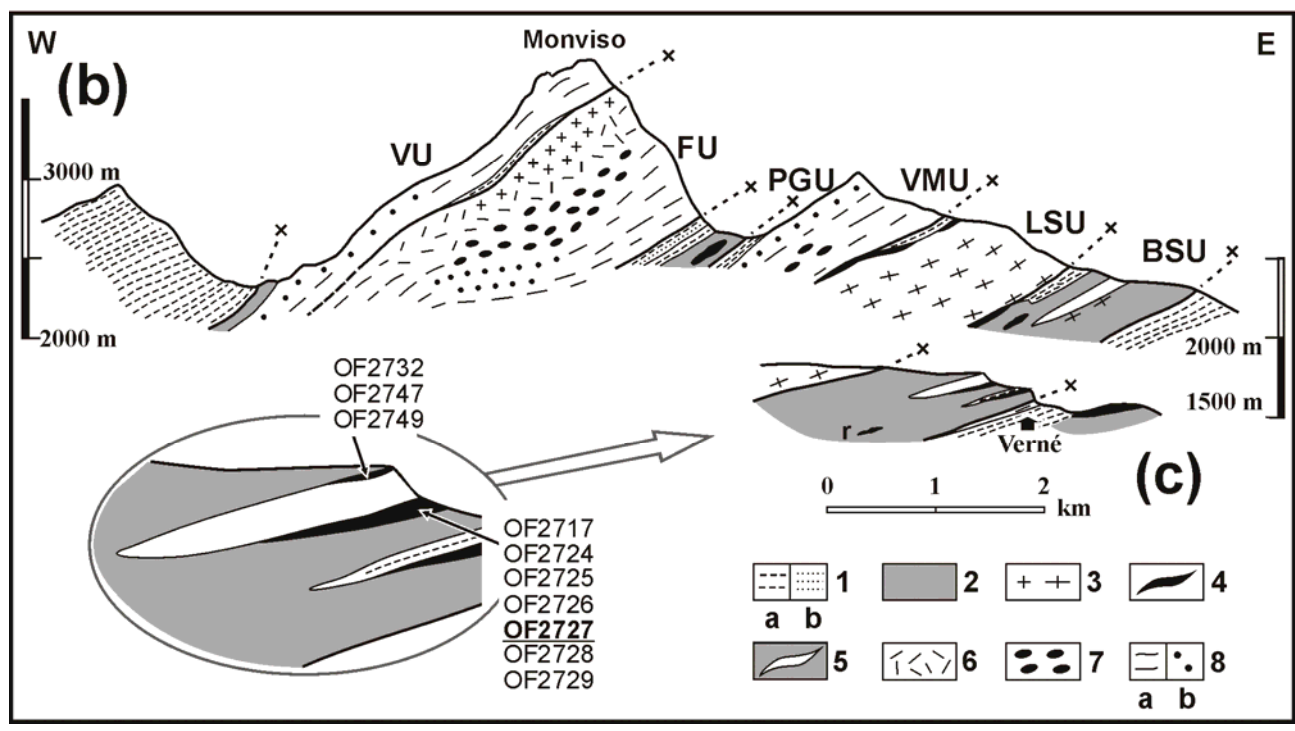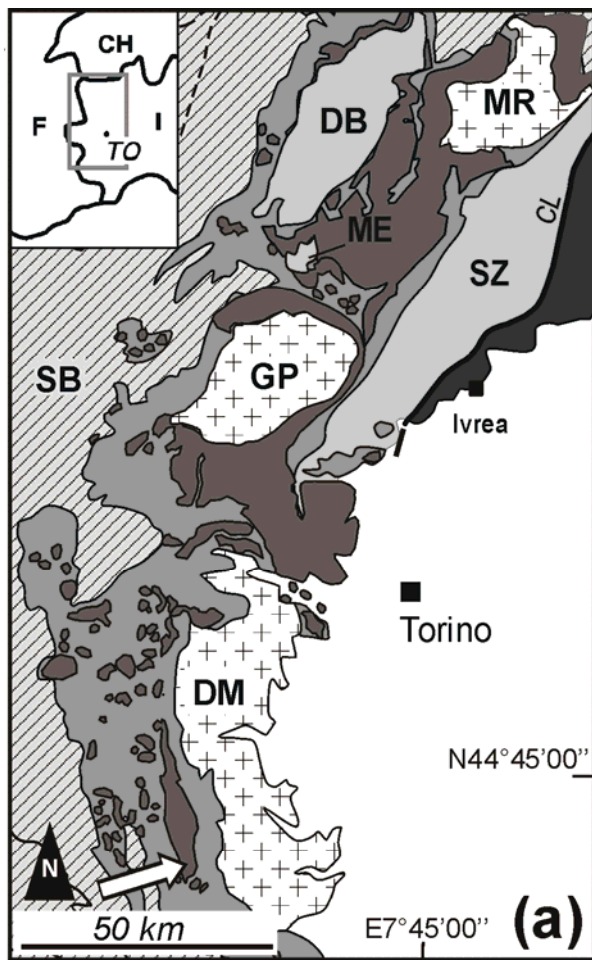
Fig. 1: (a) Simplified tectonic sketch-map of the Western Alps showing the location of the studied area (white arrow) within the Monviso metaophiolite. SB: Grand St. Bernard Zone, MR: Monte Rosa, GP: Gran Paradiso, DM: Dora-Maira; DB: Dent Blanche nappe, ME:Monte Emilius nappe,

SZ: Sesia-Lanzo Zone; CL: Canavese line. The Piemonte Zone of Calcschists with metaophiolites is reported in medium and dark grey, respectively.

(b) and (c) Schematic cross sections through the Monviso metaophiolite in the upper Valle Po (b) and along the northern side of middle Val Varaita (c). Keys to symbols are: 1a) carbonate micaschists; 1b) quartz-rich micaschists and metacherts; 2) serpentinites and antigorite schists; 3) isotropic and foliated metagabbros; 4) FeTi-oxide metagabbros and eclogites (including rodingitized varieties: r); 5) metaplagiogranites; 6) massive metabasalts; 7) pillowed metabasalts; 8a) banded metabasites; 8b) metabasites with breccia texture. VU: Vallanta Unit; FU: Forciolline Unit; PGU: Passo Gallarino Unit; VMU: Viso Mozzo Unit; LSU: Lago Superiore Unit; BSU: Basal Serpentinite Unit. The inset refers to the BSU of Val Varaita and locates the studied FeTi-oxide metagabbro OF2727 and the other FeTi-oxide metagabbro samples from the same area (modified after Castelli & Lombardo, 2007).
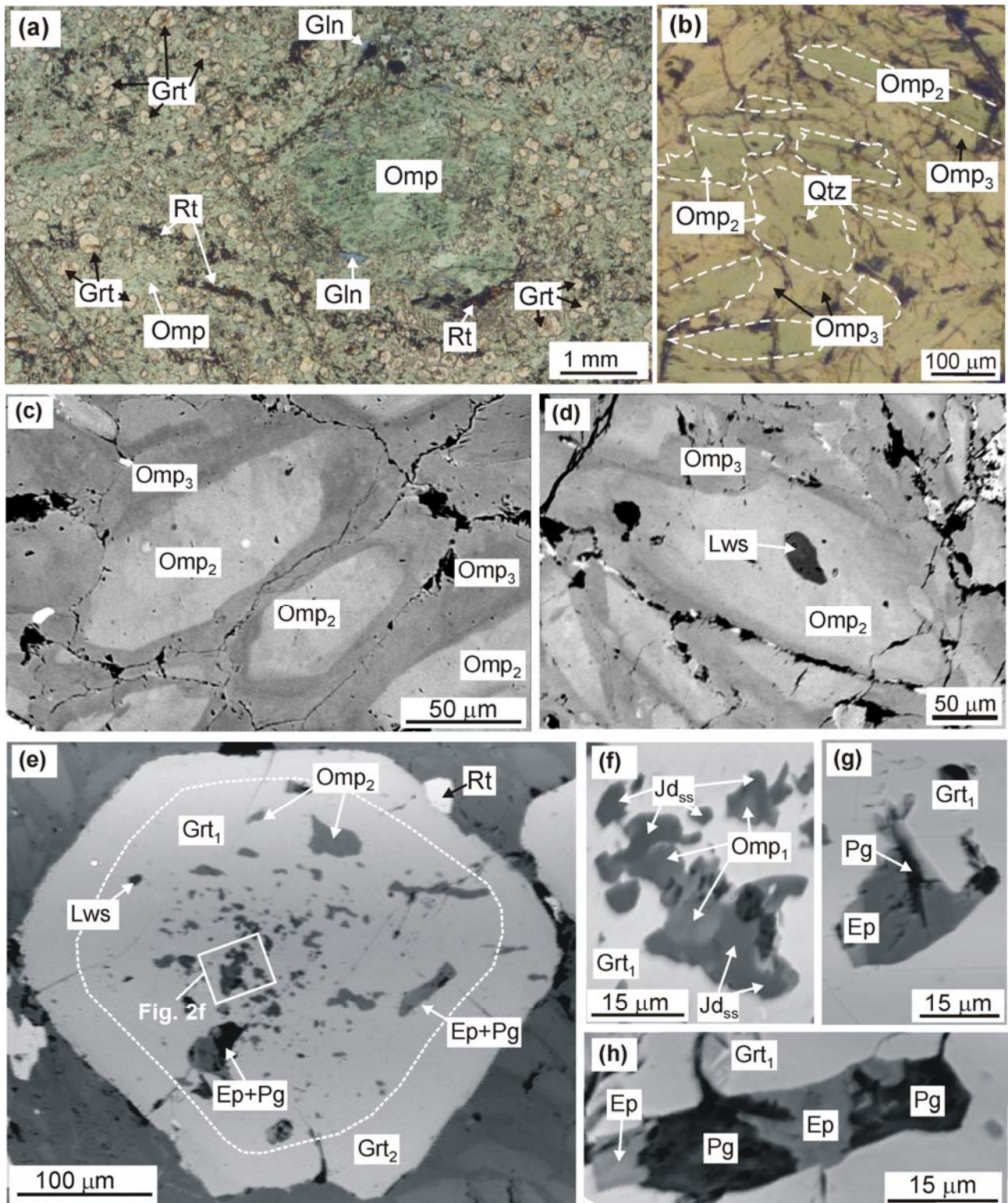
Fig. 2 – Representative microstructures of the eclogite-facies FeTi-oxide metagabbro. (a) Large igneous clinopyroxene porphyroclast, completely re-equilibrated as omphacite, set in a matrix consisting of omphacite, garnet and rutile. Rare glaucophane crystals are scattered in the matrix. Plane Polarized Light (PPL). Mineral abbreviations according to Bucher & Frey (2002). (b) Detail of the strongly zoned matrix omphacite, showing a dark green core (Omp$_2$, contoured by dashed line) and a light green rim (Omp$_3$). PPL. (c) Back-Scattered Electron image (BSE) of the zoned omphacite crystals. The lighter core (Omp$_2$) is richer in the aegirine component compared to the

darker rim (Omp_3). (d) BSE image of relic lawsonite preserved as inclusion at core of matrix omphacite. (e) BSE image of a zoned garnet crystal with the core (Grt_1) crowded of inclusions. Note lawsonite inclusions (and the epidote + paragonite pseudomorphs after lawsonite) occurring only in Grt_1. (f) Detail of the fine-grained inclusions occurring in the inner core of garnet in Fig. 2e. Jd_{ss} and Omp_1 are darker and lighter grey, respectively. BSE image. (g, h) BSE images of epidote + paragonite pseudomorphs after lawsonite, included in Grt_1.
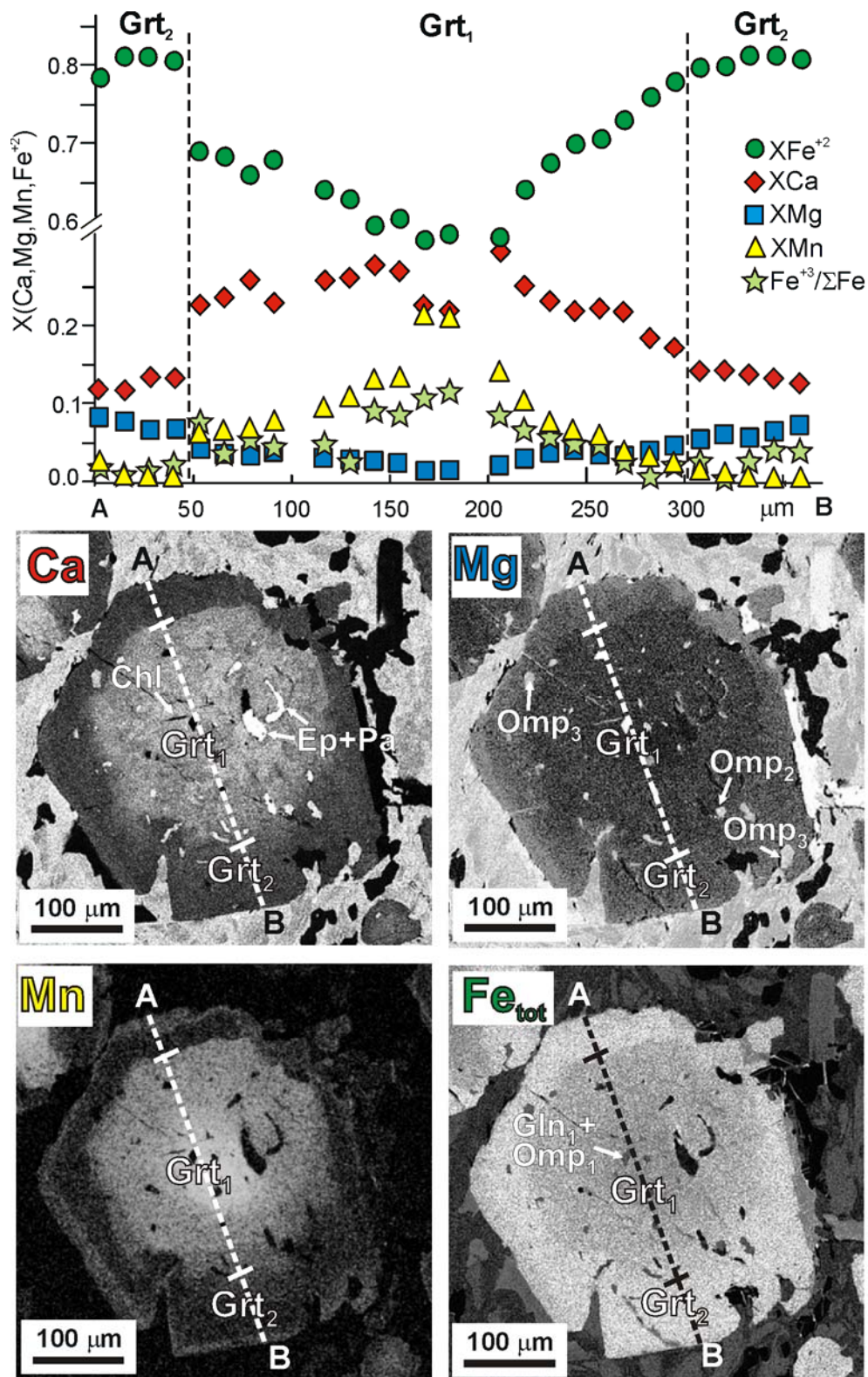
Fig. 3 − Compositional profile and Ca, Mg, Mn and Fe$_{tot}$ X-ray maps of a representative garnet crystal (see also Fig. SM3, available as Supplementary Material). In each map, lighter grey implies higher concentration, as shown by quantitative spot analyses. The dashed line in the X-ray maps locates the compositional profile.
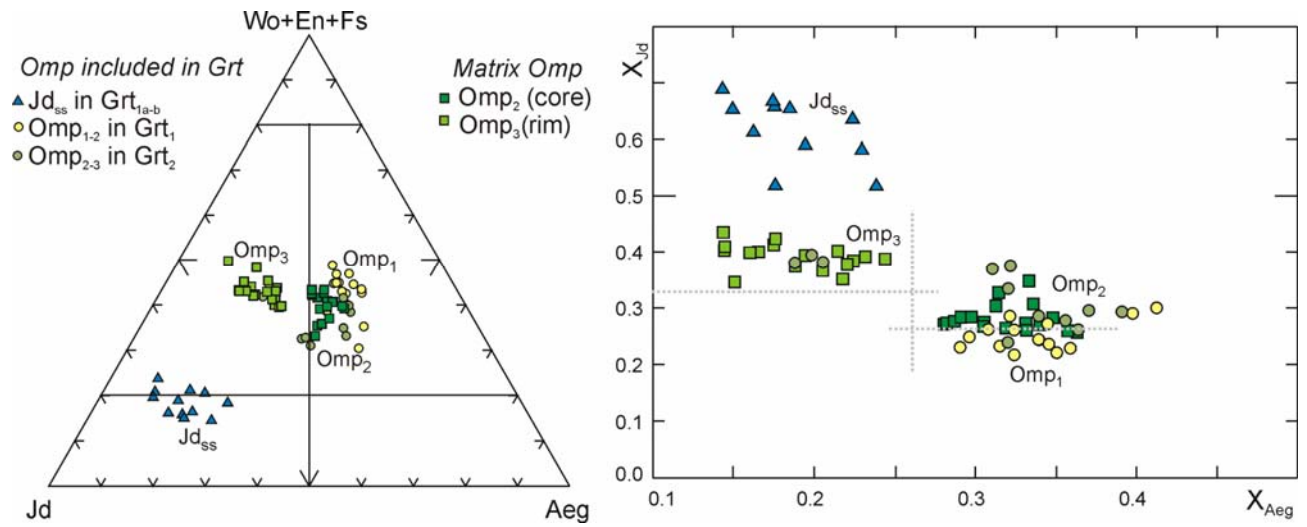
Fig. 4 – Compositions of omphacites plotted in the Morimoto *et al.* (1988) diagram and in the X_{Aeg} vs X_{Jd} diagram. $X_{Aeg} = Fe^{+3}/(Fe^{+3} + Al^{VI} + Fe^{+2} + Mg)$; $X_{Jd} = Al/(Fe^{+3} + Al^{VI} + Fe^{+2} + Mg)$.
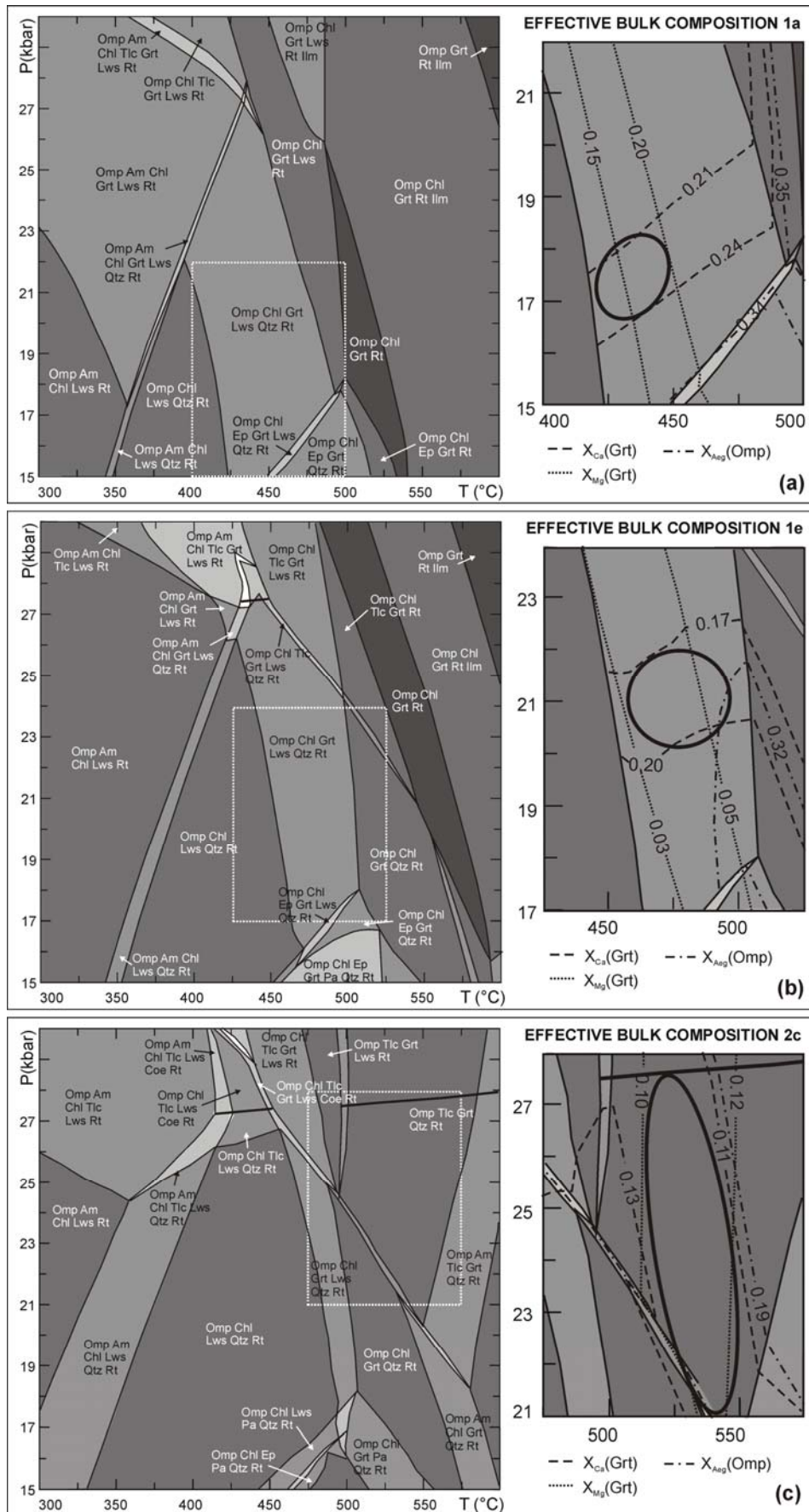
Fig. 5: *P–T* pseudosections for sample OF2727 calculated in the MnNCFMASTHO system at *a*(H₂O)=1 and XFe₂O₃=0.20 (stage I) and XFe₂O₃=0.15 (stage II), using the effective bulk

compositions calculated for stages 1a (a), 1e (b) and 2c (c) (cf. Table 4). White, light-, medium-, dark- and very dark-grey fields are tri-, quadri-, quini-, esa- and epta-variant fields, respectively. Ellipses in the insets are derived from the intersection of compositional isopleths corresponding to the actual compositions of garnet and constrain the P–T conditions of its growth at the different stages. Thick lines in Fig. 5b-c are the Qtz-Coe transition. The complete set of pseudosections for the stages 1a-1e and 2a-2c with all the compositional isopleths for garnet and omphacite is reported in Figs. SM7a-d, available as Supplementary Material.
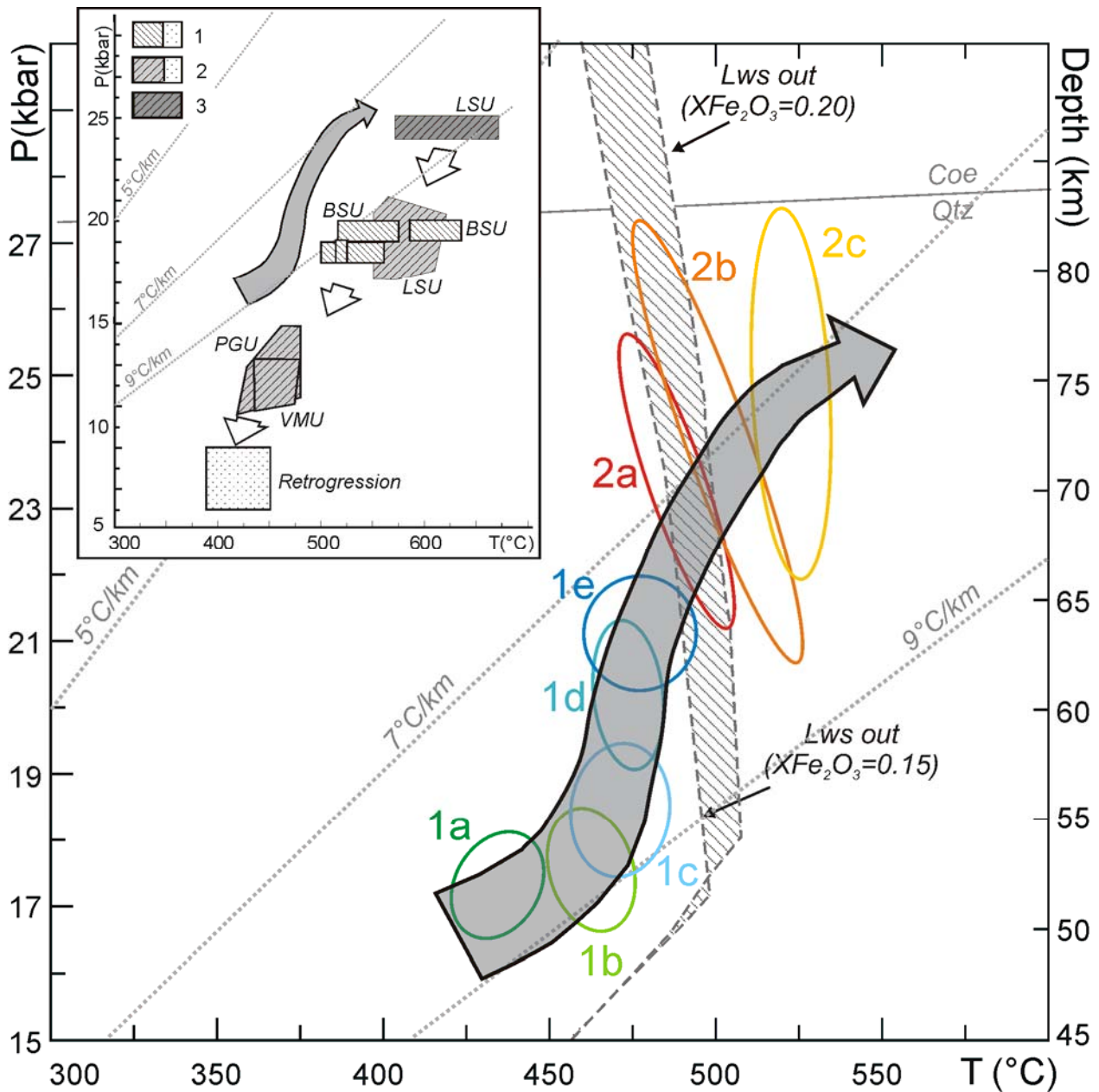
Fig. 6 – Prograde *P–T* path inferred for the studied FeTi-oxide metagabbro. The ellipses refer to *P–T* conditions constrained by pseudosection analysis for stages I (1a-1e) to II (2a-2c) (see both text and Figs. 5, and SM7a-d of Supplementary Material, for a discussion) and document a portion of the prograde *P–T* path during subduction. The dashed field marks the lawsonite breakdown as inferred from pseudosections calculated at $X(Fe_2O_3)$=0.20 and 0.15, for stage I and II, respectively. The dotted curves are thermal gradients. The inset shows the *P–T* conditions estimated by previous authors for peak (dashed fields, 1: Blake *et al.*, 1995; 2: Schwartz *et al.*, 2000; 3: Messiga *et al.*, 1999) and retrogressive (dotted field) stages in different units of the Monviso metaophiolite (abbreviations for units as in Fig. 1); the prograde *P–T* path inferred from this study is reported for comparison.
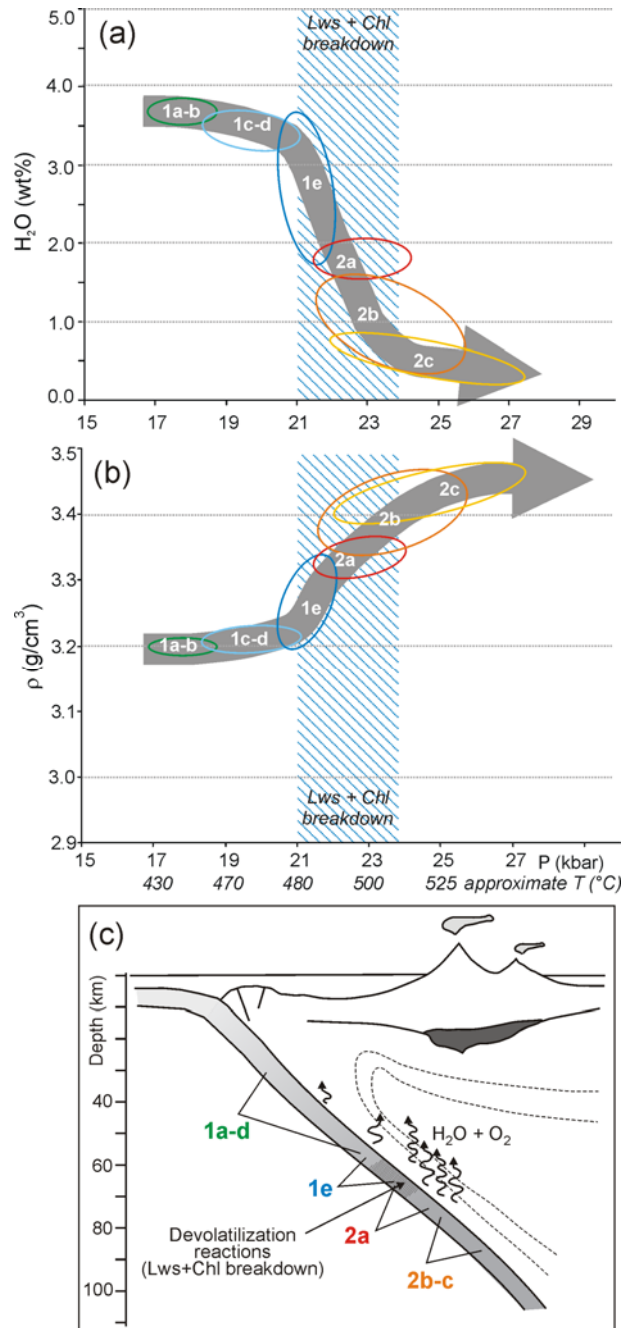
Fig. 7 – (a, b) Variations of chemical and physical properties of the FeTi-oxide metagabbro OF2727 during subduction. The dashed fields mark the lawsonite breakdown as inferred from Fig. 6. H_2O content (a) and density (b) values calculated at different metamorphic stages (I: 1a-1e; II: 2a-2c) are reported as a function of P. (c) Sketch of the different metamorphic stages (I: 1a-1e and II: 2a-2c) of metagabbro OF2727 in the subduction context. The progressively darker grey colour of the subducting oceanic crust implies higher density balanced by lower H_2O content. The dashed field along the subducting slab approximates the lawsonite and chlorite breakdown, corresponding to the depth at which the maximum H_2O and O_2 contents are released from the metagabbro into the mantle wedge.

Fig. 8 – *P–T* pseudosection calculated in the simplified system NCFMASTHO at *a*(H$_2$O)=1 and XFe$_2$O$_3$=0.20, using the effective bulk composition 1e (see Table 4), in the *P–T* range constrained for stage 1e (T=460-500°C, P=20-22 kbar). The grey field is the quini-variant Lws+Chl+Omp+Grt+Qtz+Rt field of Fig. 5b, with darker and lighter grey corresponding to higher and lower H$_2$O amounts, respectively. H$_2$O isomodes are reported as white dotted lines. Differences with respect to Fig. 5b are due to the simplified model system (see Appendix C for a discussion). Type (A) and (B) pseudo-univariant dehydration equilibria (see text for discussion) are indicated as continuous and dashed lines, respectively. Black dots are pseudo-invariant points. The listed equilibria are written such as the higher-*T* assemblages are on the right. Due to the approximation by discrete steps of the continuous variation in the composition of solid-solutions, the composition of phases in italics is the average of two or three pseudocompounds. The horizontal light grey line

at 21 kbar marks the isobaric section reported in Fig. 9. Abbreviations for solid-solution compositions are: Di=diopside, Jd=jadeite, Aeg=aegirine (hedembergite as difference to 100) for omphacite; Daph=daphnite (clinochlore as difference to 100) for chlorite; Alm=almandine, Prp=pyrope (grossular as difference to 100) for garnet.
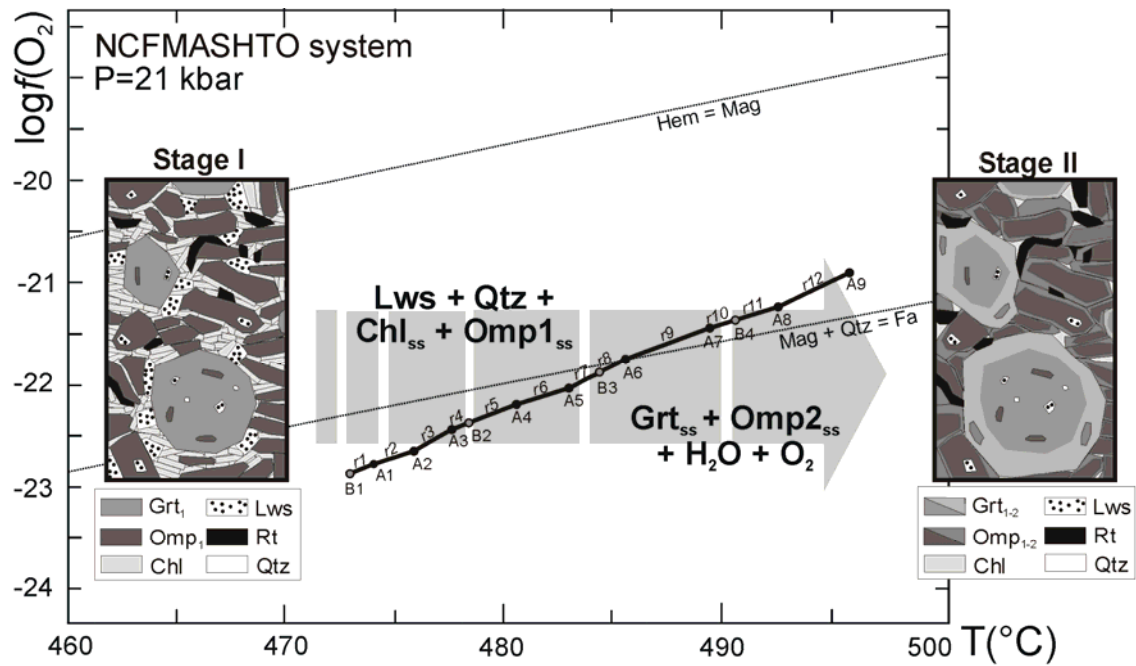
(r1) 0.2 Lws + 0.2 Qtz + 0.1 Chl(Daph64) + 14.3 $Omp_1(Di21Jd29Aeg32)$ = 0.2 Grt(Alm80Prp4) + 14.5 Omp_2(Di22Jd30Aeg30) + 0.8 H_2O + 0.1 O_2

(r2) 0.2 Lws + 0.1 Qtz + 0.02 Chl(Daph64) + 14.3 $Omp_1(Di22Jd29Aeg32)$ = 0.1 Grt(Alm80Prp4) + 14.4 Omp_2(Di22Jd30Aeg30) + 0.5 H_2O + 0.1 O_2

(r3) 0.4 Lws + 0.3 Qtz + 0.2 Chl(Daph64) + 14.5 $Omp_1(Di22Jd29Aeg32)$ = 0.5 Grt(Alm80Prp4) + 14.6 Omp_2(Di24Jd30Aeg30) + 1.6 H_2O + 0.1 O_2

(r4) 0.2 Lws + 0.2 Qtz + 0.1 Chl(Daph64) + 14.3 $Omp_1(Di23Jd29Aeg32)$ = 0.2 Grt(Alm80Prp4) + 14.5 Omp_2(Di24Jd30Aeg30) + 0.8 H_2O + 0.1 O_2

(r5) 0.5 Lws + 0.2 Qtz + 0.1 Chl(Daph60) + 24.7 $Omp_1(Di23Jd29Aeg32)$ = 0.2 Grt(Alm80Prp4) + 25.0 Omp_2(Di24Jd30Aeg30) + 1.2 H_2O + 0.1 O_2

(r6) 0.2 Lws + 0.1 Qtz + 0.02 Chl(Daph60) + 14.3 $Omp_1(Di24Jd29Aeg32)$ = 0.1 Grt(Alm80Prp4) + 14.4 Omp_2(Di24Jd30Aeg30) + 0.4 H_2O + 0.1 O_2

(r7) 0.3 Lws + 0.2 Qtz + 0.2 Chl(Daph60) + 13.7 $Omp_1(Di24Jd28Aeg32)$ = 0.4 Grt(Alm78Prp4) + 13.8 $Omp_2(Di26Jd29Aeg30)$ + 1.4 H_2O + 0.1 O_2

(r8) 0.3 Lws + 0.2 Qtz + 0.2 Chl(Daph56) + 13.9 $Omp_1(Di24Jd29Aeg32)$ = 0.4 Grt(Alm78Prp4) + 14.0 Omp_2(Di26Jd30Aeg30) + 1.3 H_2O + 0.1 O_2

(r9) 0.2 Lws + 0.1 Qtz + 0.1 Chl(Daph56) + 14.3 $Omp_1(Di25Jd29Aeg32)$ = 0.2 Grt(Alm78Prp6) + 14.5 Omp_2(Di26Jd30Aeg30) + 0.7 H_2O + 0.1 O_2

(r10) 0.2 Lws + 0.1 Qtz + 0.02 Chl(Daph56) + 14.3 $Omp_1(Di26Jd29Aeg32)$ = 0.1 Grt(Alm78Prp6) + 14.5 Omp_2(Di26Jd30Aeg30) + 0.5 H_2O + 0.1 O_2

(r11) 0.2 Lws + 0.1 Qtz + 0.02 Chl(Daph52) + 14.3 $Omp1(Di26Jd29Aeg32)$ = 0.1 Grt(Alm78Prp6) + 14.4 Omp_2(Di26Jd30Aeg30) + 0.4 H_2O + 0.1 O_2

(r12) 0.3 Lws + 0.2 Qtz + 0.2 Chl(Daph52) + 14.4 $Omp_1(Di26Jd29Aeg32)$ = 0.4 Grt(Alm78Prp6) + 14.6 Omp_2(Di28Jd30Aeg30) + 1.3 H_2O + 0.1 O_2

Fig. 9 – Isobaric T-log$f$(O_2) section in the NCFMASHTO system at P–T conditions constrained for stage 1e (i.e. average P=21 kbar and 460<T<500°C). Pseudo-invariant points A1-A9 and B1-B4 corresponds to the pseudo-univariant dehydration equilibria of Fig. 8 (see text for details), and are connected by the pseudo-univariant redox equilibria *r1-r12*. Equilibria *r1-r12* define the general redox equilibrium Lws+Qtz+Chl$_{ss}$+Omp1$_{ss}$= Grt$_{ss}$+Omp2$_{ss}$+H_2O+O_2 (the broken shape is due to the pseudocompounds approximation), which divides the T-log$f$(O_2) space in two fields (the more oxidized Lws+Qtz+Chl$_{ss}$+Omp1$_{ss}$ field, at lower T, and the more reduced Grt$_{ss}$+Omp2$_{ss}$+O_2 field, at higher T, respectively). The magnetite + quartz = fayalite and hematite = magnetite buffers are shown for comparison. The two insets schematically represent the metamorphic assemblages before (stage I) and after (stage II) the breakdown of lawsonite and chlorite. The grey arrow schematically shows the evolution from the more oxidized assemblage (stage I) to the more reduced assemblage (stage II) related to the lawsonite and chlorite breakdown. All the listed equilibria are written such as the higher-T assemblages are on the right. Due to the approximation of the continuous variation in the solid-solution compositions by discrete steps, the composition of phases in italics is the average of two or three pseudocompounds. Abbreviations for solid-solution compositions are the same as in Fig. 8.